Empirical constraints on the nucleosynthesis of nitrogen

James W. Johnson [1,2]★ David H. Weinberg,[1,2,3] Fiorenzo Vincenzo [1,2,4] Jonathan C. Bird [5]
and Emily J. Griffith [1,2]

[1]*Department of Astronomy, The Ohio State University, 140 W. 18th Avenue, Columbus, OH 43210, USA*
[2]*Center for Cosmology and Astroparticle Physics (CCAPP), The Ohio State University, 191 W. Woodruff Ave., Columbus, OH 43210, USA*
[3]*Institute for Advanced Study, 1 Einstein Dr., Princeton, NJ 08540, USA*
[4]*E.A. Milne Centre for Astrophysics, University of Hull, Cottingham Road, Kingston upon Hull HU6 7RX, UK*
[5]*Department of Physics & Astronomy, Vanderbilt University, 2301 Vanderbilt Place, Nashville, TN 37235, USA*

ABSTRACT
We derive empirical constraints on the nucleosynthetic yields of nitrogen by incorporating N enrichment into our previously developed and empirically tuned multizone galactic chemical evolution model. We adopt a metallicity-independent ('primary') N yield from massive stars and a metallicity-dependent ('secondary') N yield from AGB stars. In our model, galactic radial zones do not evolve along the observed [N/O]–[O/H] relation, but first increase in [O/H] at roughly constant [N/O], then move upward in [N/O] via secondary N production. By $t \approx 5$ Gyr, the model approaches an equilibrium [N/O]–[O/H] relation, which traces the radial oxygen gradient. Reproducing the [N/O]–[O/H] trend observed in extragalactic systems constrains the ratio of IMF-averaged N yields to the IMF-averaged O yield of core-collapse supernovae. We find good agreement if we adopt $y_N^{CC}/y_O^{CC} = 0.024$ and $y_N^{AGB}/y_O^{CC} = 0.062(Z/Z_\odot)$. For the theoretical AGB yields we consider, simple stellar populations release half their N after only $\sim$250 Myr. Our model reproduces the [N/O]–[O/H] relation found for Milky Way stars in the APOGEE survey, and it reproduces (though imperfectly) the trends of stellar [N/O] with age and [O/Fe]. The metallicity-dependent yield plays the dominant role in shaping the gas-phase [N/O]–[O/H] relation, but the AGB time-delay is required to match the stellar age and [O/Fe] trends. If we add $\sim$40 per cent oscillations to the star formation rate, the model reproduces the scatter in the gas phase [N/O]–[O/H] relation observed in external galaxies by MaNGA. We discuss implications of our results for theoretical models of N production by massive stars and AGB stars.

Key words: methods: numerical – galaxies: abundances – galaxies: evolution – galaxies: star formation – galaxies: stellar content.

1 INTRODUCTION

From a nucleosynthesis perspective, N is a unique element. Along with C and He, it is one of only three elements lighter than iron peak nuclei thought to owe a significant portion of its abundance to asymptotic giant branch (AGB) stars (e.g., Johnson 2019). N is also the primary by-product of the CNO cycle, a cyclic nuclear reaction that catalyses the conversion of H into He in stars more massive than the Sun. However, uncertainties surrounding the nucleosynthetic yields of N make it difficult to model its abundances accurately. Here, we take an empirical approach to constrain N yields by using state-of-the-art galactic chemical evolution (GCE) models to assess which functional forms describing the yield can reproduce recent observational data for gas phase abundances and trends in Milky Way-disc stars found by Vincenzo et al. (2021a).

Observationally, N abundances in external galaxies are generally measured in the gas phase and are used as a metallicity indicator because of their strong correlation with O abundances. In Fig. 1, we

present a compilation of such measurements along with data from the Milky Way:

1. H II regions in the first six CHAOS[1] galaxies: NGC 3184, NGC 628, NGC 5194, NGC 5457, M101, and NGC 2403 (Berg et al. 2020; Skillman et al. 2020; Rogers et al. 2021).
2. H II regions in nearby NGC spirals (Pilyugin et al. 2010, 'ONS' calibration).
3. H II regions in blue, diffuse star-forming dwarf galaxies (Berg et al. 2012; Izotov et al. 2012; James et al. 2015).
4. Local stars and H II regions (Dopita et al. 2016).
5. Galactic and extragalactic H II regions (Henry et al. 2000).
6. Star-forming regions in 550 nearby galaxies in the MaNGA IFU[2] survey (Belfiore et al. 2017).

Despite intrinsic scatter and some systematic variation in how the abundances are determined, this [N/O]–[O/H][3] relation is found to be similar across a wide range of astrophysical environments.

---

[1]CHAOS: CHemical Abundances Of Spirals (Berg et al. 2015).
[2]MaNGA: Mapping Nearby Galaxies at Apache Point Observatory (Bundy et al. 2015). IFU: Integral Field Unit.
[3]We follow standard notation where $[X/Y] \equiv \log_{10}(X/Y) - \log_{10}(X/Y)_\odot$.
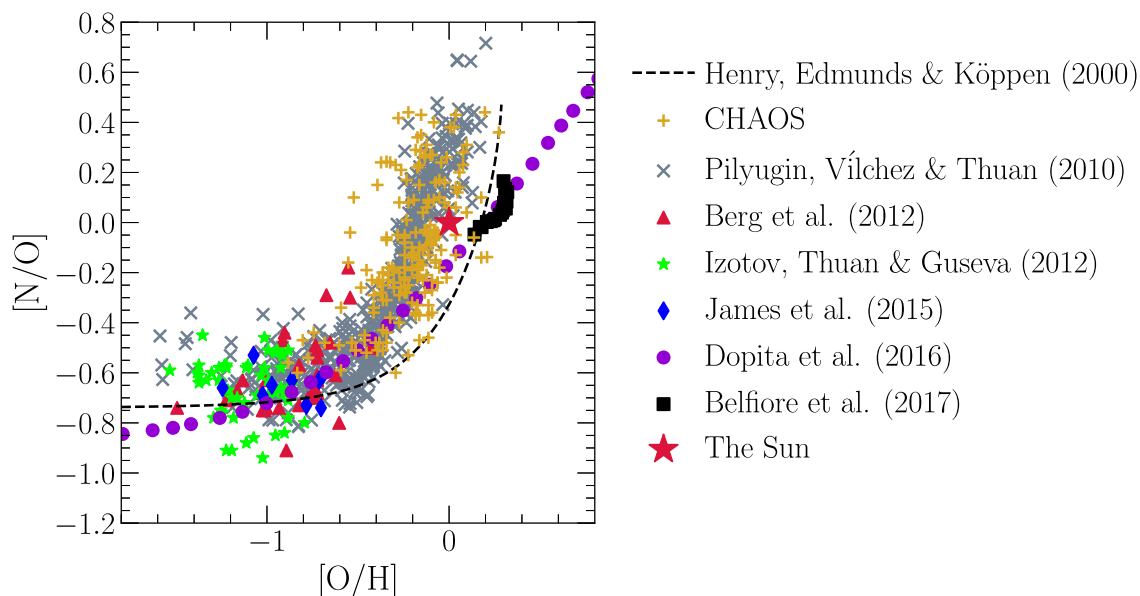
★ E-mail: giganano9@gmail.com

Figure 1. The [N/O]–[O/H] relation as observed in different galactic environments: H II regions from the first six CHAOS galaxies (golden + 's: NGC 3184, NGC 628, NGC 5194, NGC 5457, M101, and NGC 2403; Berg et al. 2020; Skillman et al. 2020; Rogers et al. 2021) and other nearby NGC spiral galaxies (grey X's; Pilyugin, Vílchez & Thuan 2010, 'ONS' calibration), H II regions in blue diffuse star-forming dwarf galaxies (red triangles: Berg et al. 2012; green stars: Izotov, Thuan & Guseva 2012; blue diamonds: James et al. 2015), in local stars and H II regions (purple circles: Dopita et al. 2016), and in the MaNGA IFU survey (black squares: Belfiore et al. 2017). The fit to [N/O] as a function of [O/H] in Galactic and extragalactic H II regions by Henry, Edmunds & Köppen (2000) is shown as a black dashed line. We omit all uncertainties for visual clarity. All data have been normalized to the Asplund et al. (2009) solar abundances, and the Sun is marked by a large red star.

Furthermore, recent arguments from both theoretical (Vincenzo & Kobayashi 2018) and observational perspectives (Hayden-Pawson et al. 2022) suggest that this relation is largely redshift-invariant. Previous studies have interpreted this consistency as an indication that the relation is nucleosynthetic in origin, reflective of a 'primary' yield that does not depend on a star's initial metal content and a 'secondary' yield that does (Vila-Costas & Edmunds 1993; van Zee, Salzer & Haynes 1998; Henry & Worthey 1999; Pérez-Montero & Contini 2009; Pilyugin, Grebel & Mattsson 2012; Andrews & Martini 2013). Although we have highlighted star-forming galaxies in Fig. 1, N abundances are also easily measured in massive ellipticals (see e.g. Schiavon 2010, Conroy 2013, and Conroy, Graves & van Dokkum 2014 for observational references), allowing it to potentially bridge the gap between the physical processes affecting galaxies of different morphologies.

The challenge in interpreting N abundances is that accurate nucleosynthetic yields from various enrichment channels remain elusive. Relative to other light elements, N synthesis is difficult to model because it is sensitive to uncertain details of stellar evolution, such as internal mixing (see discussion in, e.g., Andrews et al. 2017 and in Section 2.1 below). In this paper, we constrain N yields empirically by testing the performance of various assumptions within the framework of GCE models. To this end, we make use of the multizone model for the Milky Way published by Johnson et al. (2021), which treats the Galaxy as a series of concentric rings, describing each one as a conventional one-zone model of chemical evolution (see discussion in Section 3). This approach has been employed in the past to compute abundances for many Galactic regions simultaneously (Matteucci & Francois 1989; Wyse & Silk 1989; Prantzos & Aubert 1995; Schönrich & Binney 2009; Minchev, Chiappini & Martig 2013, 2014; Minchev et al. 2017; Sharma, Hayden & Bland-Hawthorn 2021). To ensure that our central conclusions are not affected by the model-dependent nature of the GCE framework, we consider various

parametrizations of the star formation history (SFH), the initial mass function (IMF), and the absolute scale of nucleosynthetic yields and Galactic winds. Because of the apparent universality of the [N/O]–[O/H] relation, our results using the Milky Way as a case test should apply to other galaxies as well.

At low metallicity, rotating massive stars play a key role in establishing the observed N abundances (Chiappini, Romano & Matteucci 2003; Chiappini, Matteucci & Ballero 2005; Chiappini et al. 2006; Kobayashi, Karakas & Umeda 2011; Prantzos et al. 2018; Grisoni, Matteucci & Romano 2021). Rotation plays a pivotal role in stellar evolution, inducing effects such as shear mixing, meridional circulation, and horizontal turbulence (Zahn 1992; Maeder & Zahn 1998; Lagarde et al. 2012). These effects carry internally produced C and O nuclei into the H-burning shell where they can be processed into ^{14}N via the CNO cycle (Heger & Woosley 2010; Frischknecht et al. 2016; Andrews et al. 2017). Metal-poor stars spin faster and are more compact (Maeder, Grebel & Mermilliod 1999), making these effects stronger and consequently enhancing N yields (Meynet & Maeder 2002a, b; Meynet, Ekström & Maeder 2006). We find similar results here comparing various theoretical models for massive star nucleosynthesis (see discussion in Section 2.1).

In sufficiently massive AGB stars, the base of the convective envelope is hot enough to activate proton capture reactions, allowing the CNO cycle to convert C and O isotopes into ^{14}N: a process known as hot bottom burning (HBB). AGB stars are also known to experience thermal pulses, and often these pulses are accompanied by a penetration of the convective envelope into the CO-rich core, which incorporates some of this material into the envelope itself: a process known as third dredge-up (TDU). When both processes are active, TDU adds new seed nuclei for HBB to turn into ^{14}N, substantially increasing N yields. We demonstrate in Sections 2.2 and 2.3 that various published theoretical models predict significantly discrepant N yields for high-mass AGB stars as a consequence of

differences in TDU and HBB. The differences in these processes are in turn a consequence of the uncertain assumptions built into stellar evolution models (e.g. mass-loss, opacity, convection and convective boundaries, nuclear reaction networks). In Section 4.2, we test the extent to which each of these 'off-the-shelf' yield models are able to reproduce the [N/O]–[O/H] relation in GCE models.

With a sample of 6507 galaxies from the MaNGA IFU survey (Bundy et al. 2015), Schaefer et al. (2020) demonstrate that the intrinsic scatter in the [N/O]–[O/H] relation at fixed galaxy mass is correlated with variations in the local star formation efficiency (SFE). In regions of slower star formation, [N/O] tends to be slightly higher at fixed [O/H] (see their fig. 4), which is expected from simple GCE models. In classical 'closed-box models' (e.g. Mollá et al. 2006), more AGB stars enrich the interstellar medium (ISM) with N by the time a given [O/H] is reached, whereas in 'open-box models' with inflows and outflows like the ones we present here, dilution by primordial gas accretion drives [O/H] down at fixed [N/O]. However, Schaefer et al. (2020) did not investigate stellar migration as a potential source of additional scatter in the gas-phase [N/O]–[O/H] relation. In principle, there could be a deficit or surplus of N-producing AGB stars in a given Galactic region at any time simply because the orbits are evolving, driving additional scatter in the correlation. The Johnson et al. (2021) GCE model is an ideal tool with which to test this hypothesis; the novel difference between theirs and previous models with similar motivations is that it allows stellar populations to enrich rings at different radii as they migrate. Originally developed to study the abundances of O and Fe, this aspect of Galactic evolution turned out to have an important impact on the delayed Type Ia supernova (SN Ia) enrichment of Fe, causing stochastic fluctuations in the enrichment rates with time at fixed radius. Here, we use the same methodology to test for similar effects in the delayed AGB star production of N, in turn assessing whether migration or variability in the SFE dominate scatter in the [N/O]–[O/H] relation.

With stellar abundance data, we can test the N abundances predicted by our model against observables unavailable for the gas phase, such as age and [O/Fe]. Using data from the Apache Point Observatory Galaxy Evolution Experiment (APOGEE; Majewski et al. 2017) with asteroseismic mass measurements, Vincenzo et al. (2021a) demonstrate that when stellar N abundances are corrected for internal mixing processes, the correlations with stellar age and other elemental abundances are affected. Whether or not our GCE model is able to reproduce their data constitutes a valuable test of our understanding of N nucleosynthesis and the history of N enrichment in the Milky Way. Vincenzo et al. (2021a) find good agreement between the APOGEE abundances and the Dopita et al. (2016) data, which we find to be a good representation of external galaxies as well; we therefore take the Dopita et al. (2016) trend (the purple points in Fig. 1) as our observational benchmark.

In Section 2, we discuss our adopted yields of N from its dominant nucleosynthetic sources. We discuss the details of our multizone chemical evolution model in Section 3. We describe the evolution of a fiducial model in Section 4.1. In Section 4.2, we quantify the [N/O]–[O/H] relation predicted by our model with various 'off-the-shelf' AGB star yield models taken from the literature. We investigate the relative importance of the delay-time distribution (DTD) and the metallicity-dependence of AGB star yields in Section 4.3. We compare our model predictions to stellar N abundances corrected for internal mixing processes in Section 4.4. We assess the sources of intrinsic scatter in the [N/O]–[O/H] relation in Section 4.5. We provide an analytical understanding of our key results in Section 4.6 and summarize our conclusions in Section 5.

2 NUCLEOSYNTHESIS

Here, we make use of the chemical evolution model for the Milky Way presented by Johnson et al. (2021), which runs using the publicly available Versatile Integrator for Chemical Evolution (VICE, see Appendix A; Johnson & Weinberg 2020; Griffith et al. 2021; Johnson et al. 2021), an open-source PYTHON package designed for GCE modelling. Johnson et al. (2021) focus their discussion of the model predictions on O and Fe, and we retain their yields of these elements here. The supernova (SN) yields are defined as the net mass of some element X produced over all explosion events in units of the progenitor cluster's mass. For example, with a yield of $y_X = 0.001$, a hypothetical 1000 $M_\odot$ star cluster would produce 1 $M_\odot$ of the element X instantaneously in the case of core-collapse supernovae (CCSNe) or over the DTD in the case of SNe Ia. These yields are net yields in that they do not include the metal mass ejected to the ISM that was initially present within a star; in the previous example, the 1 $M_\odot$ yield is only the newly produced metal mass. In GCE models, VICE implements an additional return of previously produced nucleosynthetic material from stellar envelopes at their birth composition (for details, see discussion in Johnson & Weinberg 2020, Johnson et al. 2021, and the VICE science documentation). We adopt the following values from Johnson et al. (2021):

(i) $y_O^{CC} = 0.015$
(ii) $y_{Fe}^{CC} = 0.0012$
(iii) $y_O^{Ia} = 0$
(iv) $y_{Fe}^{Ia} = 0.00214$,

where the subscripts and superscripts differentiate between the element and the SN type.

These choices are based on a mix of theoretical and empirical considerations. For a Kroupa (2001) IMF, the solar metallicity CCSN yields of Chieffi & Limongi (2013) and Griffith et al. (2021, based on the Sukhbold et al. 2016 models with forced explosion) predict $y_O^{CC} = 0.016$ and 0.018, respectively, if all stars from 8 to 120 $M_\odot$ explode. The value of $y_O^{CC} = 0.015$ allows for a modest amount of black hole formation but implicitly assumes that most massive stars explode.[4] While ratios of effective yields can be reasonably constrained with observed abundance ratios (e.g., Weinberg et al. 2019, 2022; Griffith et al. 2021, 2022), their absolute scale is strongly degenerate with the strength of mass-loading in Galactic winds. In GCE models, our choice of normalization leads to good agreement with the observationally inferred deuterium-to-hydrogen ratio of the local ISM (Linsky et al. 2006), while substantially lower y_O^{CC} leads to disagreement (Weinberg 2017). However, there are a number of models that reproduce observed abundance patterns of other elements in the Milky Way with weak or negligible outflows and a much lower yield normalization (e.g. Kubryk, Prantzos & Athanassoula 2015; Prantzos et al. 2018; Spitoni et al. 2019, 2021). We explore variations of the absolute scale of nucleosynthetic yields and outflows in Section 4.2.1 below and find that our conclusions are not impacted by the assumed normalization.

Our adopted values of y_O^{CC} and y_{Fe}^{CC} give [O/Fe] ≈ 0.43 for stars with pure CCSN enrichment, in good agreement with the 'high-α' plateau of disc stars found by Ramírez, Allende Prieto & Lambert (2013); matching the APOGEE plateau at [O/Fe] ≈ 0.35 (see e.g. fig. 6 of Hasselquist et al. 2021) would instead require a slightly

---

[4]If all stars from 8 to 40 $M_\odot$ explode and all more massive stars collapse, then the Sukhbold et al. (2016) models with forced explosions yield $y_O^{CC} = 0.013$ (Griffith et al. 2021).

higher $y_{Fe}^{CC} = 0.0014$. SN Ia models predict minimal O yields, justifying $y_O^{Ia} = 0$. The choice of $y_{Fe}^{Ia} = 0.00214$ then leads to good agreement with the observed [O/Fe] values of low-α thin-disc stars given the star formation assumptions used by Johnson et al. (2021, for analytical discussion, see section 3.1 of Weinberg, Andrews & Freudenburg 2017). For an Fe yield of 0.77 $M_\odot$ from a single SN Ia event (Iwamoto et al. 1999), this y_{Fe}^{Ia} corresponds to a time-integrated SN Ia rate of $R_{Ia} = 2.7 \times 10^{-3}$ $M_\odot^{-1}$ (i.e., 2.7 SNe Ia per 1000 $M_\odot$ of star formation), which is moderately higher than the value of 2.2×10^{-3} $M_\odot^{-1}$ inferred by Maoz & Mannucci (2012) for a Kroupa (2001) IMF. Our choice of yields is internally consistent and reproduces many Milky Way observations (Johnson et al. 2021), but many of the GCE model predictions would be minimally affected if we lowered y_O^{CC}, y_{Fe}^{CC}, and y_{Fe}^{Ia} by a common factor and reduced the efficiency of outflows. We return to this point in the context of N yields in Section 4.2.1.

We assume that N is not produced in significant amounts by SNe Ia (Johnson 2019), setting $y_N^{Ia} = 0$. The remainder of this section discusses the CCSN and AGB star yields of N.

A significant portion of N yields arise as a consequence of the CNO cycle. As the dominant source of pressure and energy generation in non-zero metallicity main-sequence stars with initial masses of $\gtrsim 1.3$ $M_\odot$, this cyclic nuclear reaction catalyses the conversion of H into He that would otherwise be accomplished by the proton–proton chain (von Weizsäcker 1937, 1938; Bethe 1939a, b; Adelberger et al. 2011; Suliga, Shalgar & Fuller 2021). Its slowest component by far is the $^{14}N(p, \gamma)^{15}O$ reaction (e.g. LUNA Collaboration 2006). Consequently, the first-order effect of the CNO cycle is to convert most of the C isotopes in stellar cores into ^{14}N. As we will discuss in this section, this plays an important role in shaping N yields from stars of all masses.

2.1 Core-collapse supernovae and massive star winds

In VICE, CCSN nucleosynthetic products are approximated to be produced instantaneously following an episode of star formation; this is a good approximation because the lives of massive stars are short compared to the relevant time-scales for GCE. The yield is simply the constant of proportionality between the CCSN production rate and the star formation rate (SFR):

$$\dot{M}_X^{CC} = y_X^{CC} \dot{M}_\star. \tag{1}$$

More generally, y_X^{CC} quantifies *all* of the nucleosynthetic material approximated to be produced instantaneously following a single stellar population's formation, including newly synthesized material expelled in a massive star wind before the star explodes or collapses to a black hole.

We compute theoretically predicted values of y_N^{CC} using VICE's `vice.yields.ccsne.fractional` function assuming a Kroupa (2001) IMF; details on how VICE handles these calculations can be found in section 4 of Griffith et al. (2021) and in the VICE science documentation.[5] In the left-hand panel of Fig. 2, we plot the results as a function of progenitor metallicity as predicted by the Woosley & Weaver (1995), Nomoto et al. (2013), Sukhbold et al. (2016), and Limongi & Chieffi (2018) tables. There is generally good agreement between the various non-rotating models, but only Limongi & Chieffi (2018) report yields for progenitors with non-zero rotational velocities; these yields are

substantially larger than their non-rotating counterparts, especially at low metallicity. With few seed nuclei for the CNO cycle at low Z, production of ^{14}N is difficult. Rotation-induced mixing, a highly uncertain process (Zahn 1992; Maeder & Zahn 1998; Lagarde et al. 2012), could transport newly produced C and O into the hydrogen burning shell of the CCSN progenitor, facilitating ^{14}N production (Frischknecht et al. 2016; see also discussion in section 4.2 of Andrews et al. 2017). Consequently, N yields at low metallicity are quite sensitive to model-dependent assumptions regarding stellar rotation and internal mixing processes (Heger & Woosley 2010).

We compute the [N/O] ratio of CCSN ejecta from the values of y_N^{CC} and y_O^{CC} predicted by a given yield table according to

$$[N/O]_{cc} = \log_{10}\left(\frac{y_N^{CC}}{y_O^{CC}}\right) - \log_{10}\left(\frac{Z_{N,\odot}}{Z_{O,\odot}}\right), \tag{2}$$

where $Z_{X,\odot}$ is the abundance by mass of some element X in the sun, for which we take $Z_{N,\odot} = 6.91 \times 10^{-4}$ and $Z_{O,\odot} = 5.72 \times 10^{-3}$ based on the photospheric measurements of Asplund et al. (2009). For each value of y_N^{CC} in the left-hand panel of Fig. 2, we compute the corresponding values of y_O^{CC} and illustrate the resultant [N/O]$_{cc}$ ratios in the right-hand panel. These yield ratios follow similar trends with progenitor metallicity and rotation as y_N^{CC} itself, a consequence of the fact that these studies predict relatively metallicity- and rotation-independent O yields. At low metallicity, CCSN yields of N dominate over the AGB star yields (see discussion in Section 2.2), and Fig. 1 suggests a plateau in [N/O] at low metallicity at [N/O]$_{cc} \approx -0.7$. We have examined versions of Fig. 2 with shallow and steep variations of the Kroupa (2001) IMF (i.e. power-law indices $\gamma = -2.0$ and -2.6, respectively). This level of IMF variability produces factor of ~ 2 variations in y_N^{CC}, but the [N/O]$_{cc}$ ratios are nearly unaffected because massive star yields of N and O follow similar trends with stellar mass. Taking this value in combination with our adopted O yield of $y_O^{CC} = 0.015$, equation (2) suggests that $y_N^{CC} = 3.6 \times 10^{-4}$. We highlight both [N/O]$_{cc} = -0.7$ and $y_N^{CC} = 3.6 \times 10^{-4}$ with horizontal black dashed lines in Fig. 2, finding good agreement with the rotating progenitor models of Limongi & Chieffi (2018) in both panels. This indicates that rotating massive stars play an important role in establishing the N abundances at low metallicity, in agreement with previous works (Chiappini et al. 2003, 2005, 2006; Kobayashi et al. 2011; Prantzos et al. 2018; Grisoni et al. 2021). However, we cannot tightly constrain the rotation rates of massive stars here since yield tables are available at only three values. We therefore take $y_N^{CC} = 3.6 \times 10^{-4}$ as our fiducial CCSN yield of N; both the normalization and metallicity-independence of this choice are supported by the Limongi & Chieffi (2018) models.

The Sukhbold et al. (2016) tables, available only at solar metallicity, agree nearly perfectly with our empirical value of $y_N^{CC} = 3.6 \times 10^{-4}$, but they predict a higher value of [N/O]$_{cc}$ by ~ 0.2 dex. This is a consequence of the failed supernovae incorporated into their model and the lowered values of y_O^{CC} that result (see discussion in Section 4.2). While N emerges in substantial amounts in winds, much of the O produced by massive stars is ejected during the explosion, making the O yield more sensitive to the black hole landscape (Griffith et al. 2021). Most of the SN models plotted in Fig. 2 estimate slightly higher [N/O]$_{cc}$ at $\log_{10}(Z/Z_\odot) = 0$ relative to our empirical value of [N/O]$_{cc} = -0.7$, but they still fall short of solar [N/O]. This implies the need for an additional enrichment channel, which is expected because it is well understood that N is
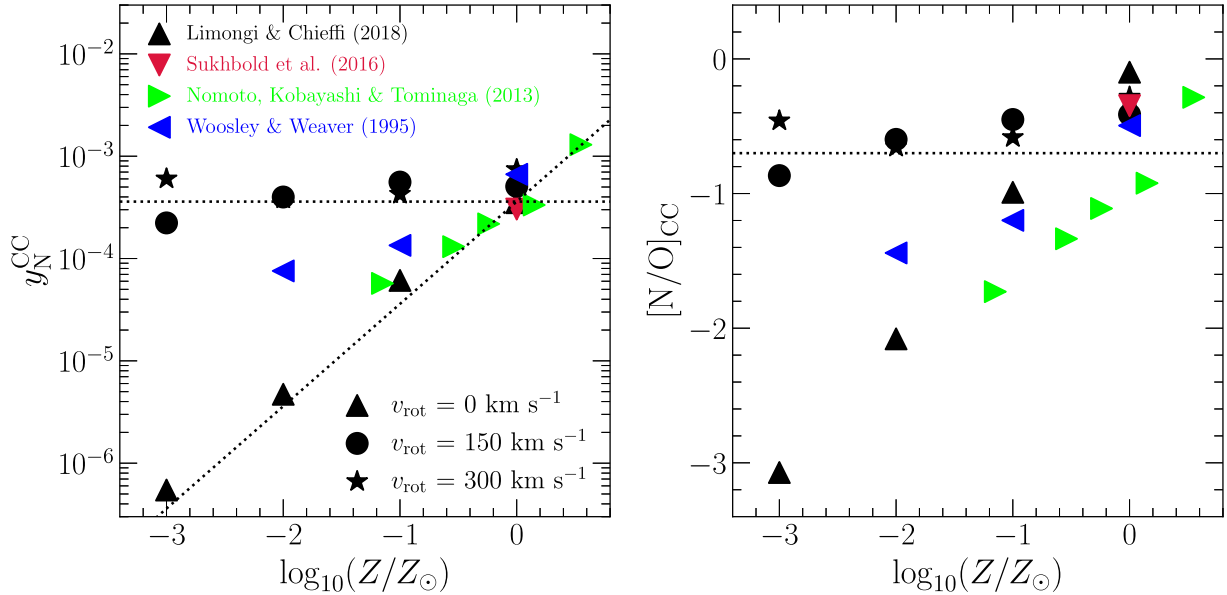
Figure 2. Left: IMF-averaged CCSN yields of N calculated using VICE's vice.yields.ccsne.fractional function with the tables published by Woosley & Weaver (1995, blue), Nomoto, Kobayashi & Tominaga (2013, green), Sukhbold et al. (2016, red), and Limongi & Chieffi (2018, black). All studies report yields for non-rotating progenitors, shown by the triangles; for visual clarity, the triangles point in a different direction for each study according to the legend. Limongi & Chieffi (2018) report additional yields for progenitors with rotational velocities of 150 (circles) and 300 km s^{-1} (stars). The horizontal dashed line marks $y_N^{CC} = 3.6 \times 10^{-4}$, the value of our fiducial CCSN yield of N in our GCE models. We also use the form shown by the slanted line (equation 8) in Section 4.2.2 in combination with some of our AGB star yield models discussed in Section 2.2. Right: The [N/O] ratio predicted by each of the explosion models in the left-hand panel, under the same colour coding and marker scheme. We mark the position of [N/O] = −0.7 with a black dotted line, the value roughly suggested by the observations of low-metallicity systems highlighted in Fig. 1.

also produced in considerable amounts by AGB stars (e.g. Johnson 2019).

2.2 Asymptotic giant branch stars

We use Y_X^{AGB} to denote the fractional net yield of an AGB star of mass $M_\star$, so that the mass yield is $M_\star Y_X^{AGB}$. We then define the IMF-averaged yield y_X^{AGB} by integrating over the mass range $M_\star = 1$–8 M$_\odot$. Enrichment proceeds as it does in Johnson et al. (2021): AGB stars place their nucleosynthetic products in the $\delta R_{gal} = 100$ pc ring that they are in at a given time, allowing stars to enrich distributions of radii as they migrate. VICE implements an algorithm that computes the mass in dying stars from each stellar population, and the zero age main-sequence (ZAMS) mass required to compute the fractional yield comes from a mass–lifetime relationship. For the latter, we adopt the metallicity-independent parabola in $\log \tau$–$\log m$ space from Larson (1974) with updated coefficients from Kobayashi (2004) and David, Forman & Jones (1990, see discussion of the mass–lifetime relationship in VICE in Appendix A).

We make use of four previously published tables of AGB star N yields computed from stellar evolution models, each of which are sampled on a grid of progenitor masses and metallicities. To approximate the net yield Y_X^{AGB} as a smooth function of $M_\star$ and $Z_\star$, VICE interpolates bi-linearly – once in mass M and once in metallicity Z – and linearly extrapolates above or below the grid in either quantity as necessary. By comparing the predicted abundances of the Johnson et al. (2021) Milky Way model to the latest observational data, we can constrain how accurately these 'off-the-shelf' yield models characterize N production. These models taken from the literature are as follows:

(i) Karakas (2010, hereafter K10)[6] published yields for $Z = 0.0001$, 0.004, 0.008, and 0.02 progenitors. We plot these yields in the upper left panel of Fig. 3.

(iii) Karakas & Lugaro (2016) and Karakas et al. (2018) published yields for $Z = 0.0028$, 0.007, 0.014, and 0.03 progenitors; we hereafter refer to these yields as the KL16 + K18 model. We illustrate these yields in the upper middle panel of Fig. 3.

(iv) We combine the yields for $Z = 0.0003$ and 0.008 progenitors from Ventura et al. (2013) with those at $Z = 0.004$ from Ventura et al. (2014), at $Z = 0.014$ from Ventura et al. (2018), and at $Z = 0.04$ from Ventura et al. (2020) into a single table of yields. In this set, we also include a set of un-published yields at $Z = 0.001$ and 0.002 computed from similar models (provided by P. Ventura, private communication). We hereafter refer to this yield set as the V13 model, and we plot a subsample of these yields in the upper right panel of Fig. 3.

(v) The default set of AGB star yields in VICE is taken from Cristallo et al. (2011, 2015), who published yields for $Z = 0.0001$, 0.0003, 0.001, 0.002, 0.003, 0.006, 0.008, 0.01, 0.014, and 0.02 progenitors. We hereafter refer to these yields as the C11 + C15 model, and we illustrate a subsample of them in the lower left panel of Fig. 3.

VICE also allows users to construct their own functions of progenitor mass and metallicity to describe the AGB star yield. Motivated by the roughly linear nature of the C11 + C15 yields and their general success once renormalized by a constant factor (see discussion in Section 4.2), we construct a model in which the yield is

---

[6]We clarify that our abbreviations of each of these papers refer specifically to their yields of N as we adopt them in our model. We cite the full names of these papers when referring to their more general results.
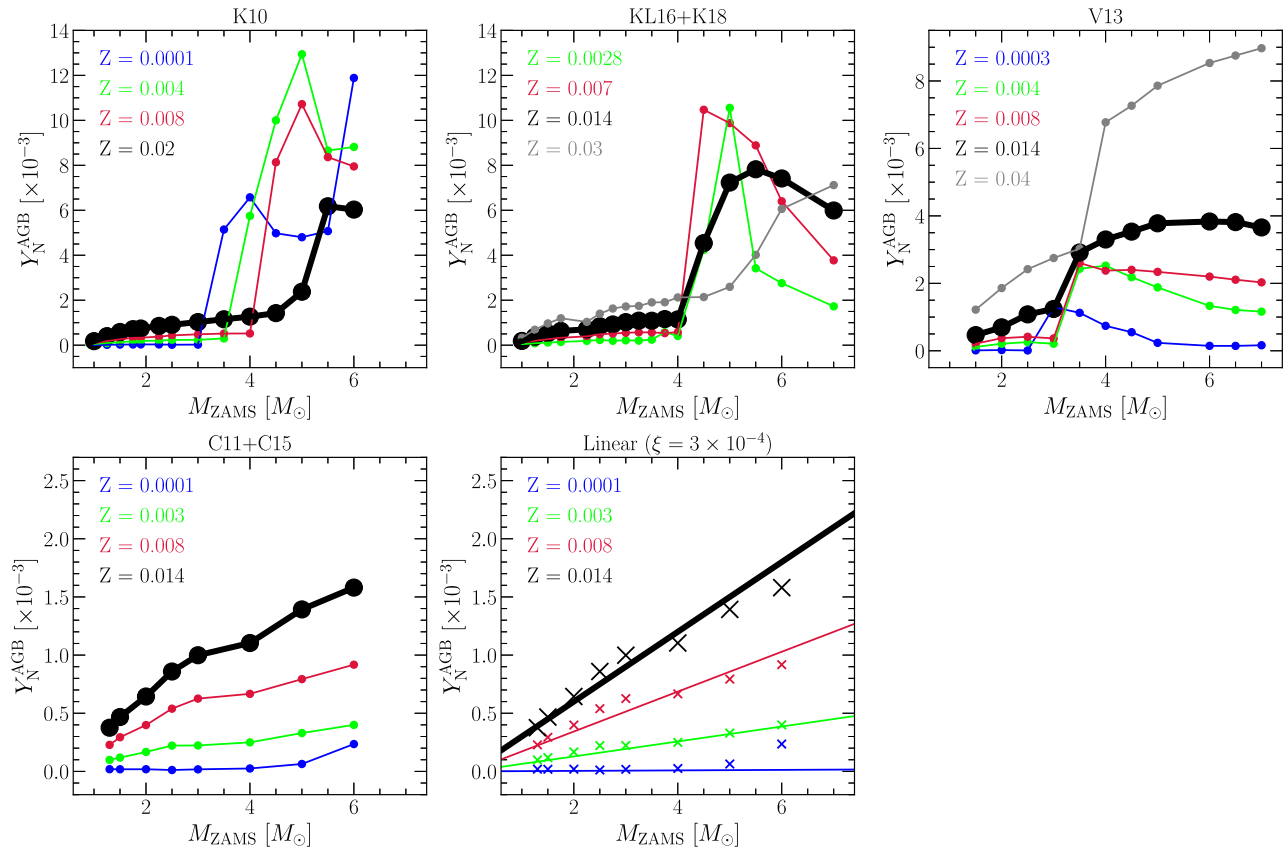
Figure 3. The fractional yields of N from AGB stars Y_N^{AGB} as a function of progenitor ZAMS mass and birth metallicity Z as reported by Karakas ([2010](#), upper left), Karakas & Lugaro ([2016](#)) and Karakas et al. ([2018](#), upper middle), Ventura et al. ([2013](#), [2014](#), [2018](#), [2020](#), upper right), and Cristallo et al. ([2011](#), [2015](#), lower left). For Ventura et al. ([2013](#), [2014](#), [2018](#), [2020](#)) and Cristallo et al. ([2011](#), [2015](#)), we show the yields only for a selection of metallicities available from their provided tables. We highlight yields at solar metallicity ($Z = 0.02$ for Karakas [2010](#), $Z = 0.014$ otherwise) with bold black lines. In the lower right panel, we show our linear model (coloured lines, see equation [3](#)) in comparison to the Cristallo et al. ([2011](#), [2015](#), coloured X's) predictions. We caution that the y-axis ranges are not the same between panels in this figure.

linearly proportional to both progenitor ZAMS mass and metallicity:

$$Y_N^{AGB} = \xi \left(\frac{M_\star}{M_\odot} \right) \left(\frac{Z_\star}{Z_\odot} \right). \tag{3}$$

We illustrate this model in the lower middle panel of Fig. 3 for $\xi = 3 \times 10^{-4}$ in comparison to the C11 + C15 yields shown by the coloured X's. Although we find good agreement between the C11 + C15 yields and our linear model with a normalization of $\xi = 3 \times 10^{-4}$, for our fiducial AGB star yield of N we take a slope of $\xi = 9 \times 10^{-4}$. We discuss the absolute scaling of our nucleosynthetic yields in Section 4.2 below.

As is clear from Fig. 3, the N yields reported by these studies show substantial differences. Unfortunately, ascertaining the origin of these differences is difficult because each model employs its own assumptions for important evolutionary parameters such as opacity, mass-loss, nuclear reaction networks, and convection and convective boundaries within stars, all of which have a significant impact on stellar evolution and thus the predicted yields (Karakas & Lattanzio [2014](#); Karakas & Lugaro [2016](#); Ventura et al. [2016](#), [2018](#)). However, the differences can be qualitatively understood by considering two important phenomena known to occur within AGB stars: TDU[7] and HBB. The variations in how TDU and HBB proceed

between different stellar evolution models arise as consequences of the different input physics.

When an AGB star experiences a thermal pulse, this is usually accompanied by a TDU event whereby the convective envelope penetrates into the hydrogen-depleted core, mixing some of this material with other material exposed to partial He-shell burning. The $^{13}C(\alpha, n)^{16}O$ reaction, which is the main source of free neutrons in low-mass AGB stars (Gallino et al. [1998](#)), can occur at substantial rates when this core material is mixed with the He-rich shell. This process does not directly affect N abundances in the shell because the core is mostly composed of C and O at this evolutionary phase, but ^{14}N plays an important role in shaping an AGB star's overall s-process yield by acting as an efficient catalyst of neutron decay via the $^{14}N(n, p)^{14}C(\beta^+ \nu_e)^{14}N$ reaction, the first step of which is a resonant neutron capture (Cristallo et al. [2011](#)).

HBB refers to proton capture reactions at the base of the convective envelope, activating the CNO cycle and producing large amounts of ^{14}N at the expense of C and O isotopes (e.g. Scalo, Despain & Ulrich [1975](#); Bloecker & Schoenberner [1991](#)). HBB requires a minimum temperature slightly above 10^7 K at the base of the convective envelope (e.g. Sackmann & Boothroyd [1991](#)), which in

---

[7]The time adverbial 'third' in TDU refers only to the fact that these dredge-up episodes are occurring while the star is on the asymptotic giant branch.

Because they are associated with the thermal pulsations of AGB stars, there are many episodes of third dredge-up.

turn requires a high mass AGB star progenitor. For comparison, HBB occurs in the Karakas (2010) models for solar metallicity stars at $M_{ZAMS} = 4$–5 $M_\odot$ and up, whereas TDU occurs at $M_{ZAMS} = 2$–2.5 $M_\odot$ and up. The minimum mass for both decreases at lower metallicities because these stars are both hotter and more compact.

The most efficient N production occurs when both TDU and HBB are active within an AGB star, because each replenishment of C and O isotopes by TDU adds new seed nuclei for the CNO cycle with HBB. This is the reason for the substantial increase in yields at ∼4 $M_\odot$ in the K10 and KL16 + K18 models; in both yield sets, every star that experiences HBB also experiences TDU (see, e.g., table 1 of Karakas 2010). Their high mass AGB star yields are higher at low Z because both HBB and TDU are more efficient (see discussion in Ventura et al. 2013): when the metallicity is low, each TDU episode is deeper due to the lower opacity, and the base of the convective envelope is hotter, increasing the rate of CNO cycle reactions in HBB. This interaction between TDU and HBB is also the reason for the increase in the V13 yields near ∼3 $M_\odot$, but unlike the K10 and KL16 + K18 models, their stars experience both processes only in this narrow range of mass.

Of all of these yields taken from the literature, the C11 + C15 sample shows the smoothest dependence on progenitor mass and metallicity. Below ∼3 $M_\odot$, their agreement with the KL16+K18 yields is good, but this model has much lower N yields for higher mass AGB stars. Pinpointing a single reason for this difference is difficult, even when considering the differences between HBB and TDU. Relative to the KL16 + K18 yields (see discussion in section 5 of Karakas & Lugaro 2016), the C11 + C15 stars have more mass-loss, fewer thermal pulses overall, and weaker HBB due to a lower temperature at the base of the convective envelope. Each of these effects lower the yield of ^{14}N, but the latter is the dominant one.

Although the K10 and KL16 + K18 yield models both show a substantial increase in N yields above ∼4 $M_\odot$, there are some noteworthy differences between the two. In the newer version, the yields at solar metallicity are somewhat higher, and the yields at sub-solar metallicities decreased slightly, particularly for the highest mass AGB stars. These differences can be understood by slight variations in the input physics (A. Karakas, private communication). A portion of the increase in the yields at solar metallicity can be attributed to the assumption of $Z_\odot = 0.02$ versus $Z_\odot = 0.014$[8] and the impact this has on both HBB and TDU, but it does not account for the entire difference. These stars are also slightly hotter and more compact due to updated opacity tables, giving them hotter HBB and deeper TDU. With more thermal pulses overall and therefore a longer AGB lifetime, these stars have more time to convert ^{12}C into ^{14}N. KL16 + K18 also use low-temperature opacity tables based on Marigo (2002) that follow the surface composition of the star more closely. These opacities are high, making the $Z = 0.007$ AGB stars larger and increasing the mass-loss rate relative to K10, truncating their N yields, particularly at the highest masses. The $Z = 0.0028$ model uses the Bloecker (1995) mass-loss prescription rather than that of Vassiliadis & Wood (1993), which was used for the K10 yields as well as the yields at other metallicities in the KL16 + K18 model. This choice results in fewer

thermal pulses and a shorter AGB lifetime, giving them less time to process C and O nuclei into ^{14}N.

We do not discuss the AGB star yields of O and Fe here as these quantities are negligible compared to their SN yields. Although we focus our investigation on AGB yields from ≲7 $M_\odot$ stars, slightly more massive stars (up to ∼12 $M_\odot$) sit near the critical mass boundaries between different types of massive white dwarfs and electron capture SN progenitors. Doherty et al. (2017) investigated theoretically predicted yields of these stars and found significant production of CNO isotopes. There is also the intriguing possibility of the CNO yields from the earliest, most metal-poor AGB stars (e.g., the $Z = 10^{-5}$ models of Gil-Pons et al. 2013, 2021) and the insight this may afford into N production at low Z and the most metal-poor stars in the Galaxy. While experiments with such yields in our GCE models would be interesting, this is beyond the scope of the current paper since our AGB yield models already span a wide range of assumptions regarding stellar evolution.

2.3 IMF-averaged AGB star yields: metallicity and time dependence

To more directly compare these AGB star yields predicted from stellar evolution models, we plot their IMF-weighted yields at solar metallicity in the left-hand hand panel of Fig. 4. We assume $Z_\odot = 0.014$ based on Asplund et al. (2009) and Asplund, Amarsi & Grevesse (2021); since the K10 model reports yields at $Z = 0.02$ rather than $Z = 0.014$, we simply interpolate linearly to $Z = 0.014$ in the same manner that VICE does in our GCE models. As mentioned in Section 2.2, the AGB star yield Y_N^{AGB} as we have parametrized it is in units of the progenitor star's ZAMS mass, and consequently the *mass yield* of N is given by $M_\star Y_N^{AGB}$. With an additional weight of $M_\star^{-2.3}$ from the IMF in this mass range (e.g. Kroupa 2001), we therefore multiply the values of Y_N^{AGB} by $(M_\star/M_\odot)^{-1.3}$ to quantify a star's relative contribution to the total N yield taking into account the intrinsic mass distribution.[9] With the additional weight of $M_\star^{-1.3}$, the C11 + C15 yields are relatively mass-independent. For the other yield models, higher mass AGB stars dominate the overall yield due to the effects of TDU and HBB discussed in Section 2.2.

Using VICE's `vice.single_stellar_population` function, in the middle panel of Fig. 4 we plot the total N yield as a function of age from a single stellar population. For the sake of this calculation, we set all CCSN yields of N to zero in order to highlight the AGB star contribution. We show the results of this procedure for solar metallicity only, and we normalize all values to the total mass produced at $t = 13.2$ Gyr (the total amount of time our GCE model is integrated over; see discussion in Section 3). Under the C11 + C15 yields, it takes ∼250 Myr for a single stellar population to produce ∼50 per cent of its N from AGB stars, as noted by the coloured points at the top of the panel. This is in good agreement with Maiolino & Mannucci (2019), who find that similar parameter choices predict 80 per cent of the N yield to be ejected within ∼1 Gyr (see their fig. 1). The characteristic time-scales for N production are even shorter in the other yield models because of their more pronounced contributions from massive stars with short lifetimes (e.g. Larson 1974; Maeder & Meynet 1989; Padovani & Matteucci 1993). For comparison, we plot the enrichment of Fe by our $t^{-1.1}$ power-law DTD, also with the CCSN yield set to zero to highlight the delayed component. The characteristic delay time for

---

[8]Changes in the accepted value of the metallicity of the sun trace back to the canonical value of ∼2 per cent derived by, e.g., Anders & Grevesse (1989) and Grevesse & Sauval (1998), later being revised to ∼1.4 per cent by, e.g., Lodders (2003) and Asplund, Grevesse & Sauval (2005). See table 4 of Asplund et al. (2009) for a compilation of measured values.

[9]This weight gives a contribution per linear interval of M_{ZAMS}, so one can use area under the curve to assess relative contributions.
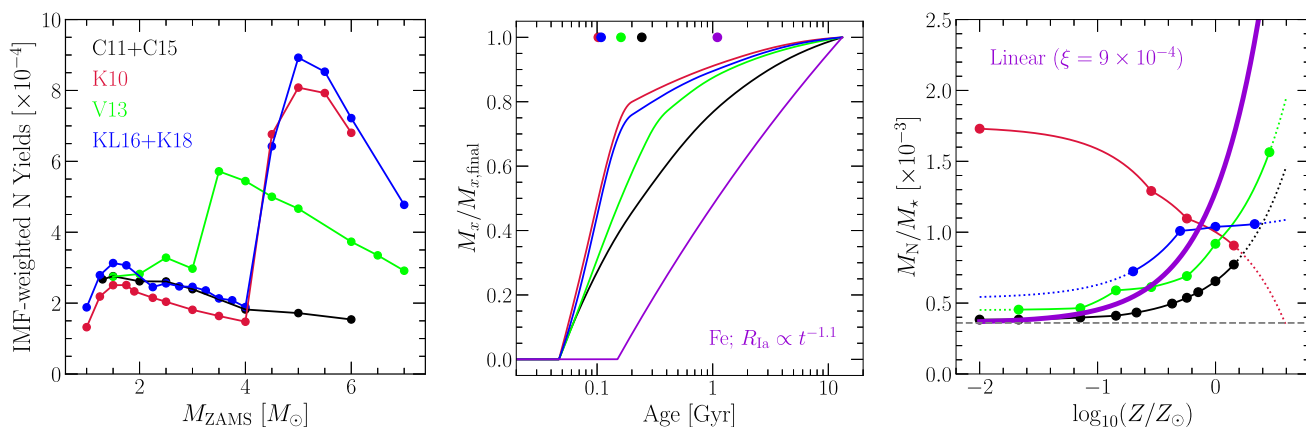
Figure 4. Left: The IMF-weighted mass yield of N from AGB stars as a function of progenitor ZAMS mass at solar metallicity (i.e., the contribution per linear interval dM_{ZAMS}; $Z_\odot = 0.014$). Middle: The net mass of N produced by AGB stars from a single stellar population for each of our yield models at solar metallicity. The purple line denotes the same for Fe assuming our $t^{-1.1}$ DTD as in the Johnson et al. (2021) chemical evolution model. All values are normalized to the total mass produced at an age of 13.2 Gyr. Points at the top of the panel denote the ages at which 50 per cent of the total mass yield has been produced. Right: The total amount of N produced by a 13.2 Gyr old stellar population as a function of metallicity for each of our yield models normalized by the stellar population's initial mass. Points mark metallicities at which the published tables report yields, and the lines are dotted at metallicities that are above (below) the maximum (minimum) metallicity reported by a given study (i.e., where extrapolation is necessary). In this panel only, we include the metallicity-independent contribution $y_N^{CC} = 3.6 \times 10^{-4}$ from CCSNe (gray dashed line). The bold purple curve represents our inference of the *total* N yield (CCSN + AGB) required to reproduce the observational constrains discussed in Section 4 given our adopted O and Fe yields (Section 2).

Fe production is considerably longer than that of N – up to an order of magnitude depending on which yield model is adopted. As noted in Johnson et al. (2021), a characteristic delay time of ~1 Gyr is exactly as expected for an $\sim t^{-1}$ DTD because half of the SN Ia events occur between 100 Myr and 1 Gyr and the other half between 1 and 10 Gyr.

A characteristic delay time of only ~250 Myr may seem surprising given the relatively mass-independent nature of the IMF-weighted C11 + C15 yields. This arises out of the steep nature of the stellar mass–lifetime relation (e.g. Larson 1974; Maeder & Meynet 1989; Padovani & Matteucci 1993). For example, 2 and 3 $M_\odot$ stars live only ~1.2 Gyr and ~400 Myr, respectively, and over the course of 13.2 Gyr, only stars of masses $\gtrsim0.9$ $M_\odot$ will have enough time to finish their hydrogen burning. Consequently, most of the mass range of stars that will evolve through an AGB phase will do so within the first few hundred Myr after their formation, and with mass-independent IMF-weighted yields, this accounts for most of the N. We clarify that the delay times computed here apply *only* to N and not necessarily to other elements produced by AGB stars. As we have illustrated here, the effective DTD of AGB star enrichment is dictated by the combination of the stellar mass–lifetime relation and the mass dependence of the yield, which should in principle differ from element to element. Other elements produced by slow neutron capture often have the highest yields from lower mass AGB stars. For example, Cristallo et al. (2011, 2015) report Sr yields that are dominated by $M_{ZAMS} = 2$–3 $M_\odot$ progenitors (see fig. 5 of Johnson & Weinberg 2020), giving it a characteristic delay time of ~500 Myr. The characteristic delay-times will be as long as a few Gyr if and only if the yields are dominated by $\lesssim1.5$ $M_\odot$ stars.

In the right-hand panel of Fig. 4, we plot the total amount of N produced by a 13.2 Gyr old single stellar population as a function of its initial metallicity according to all of our AGB star yield tables, including the linear model (see equation 3 and discussion in Section 2.2). For this calculation, we include the metallicity-independent CCSN yield ($y_N^{CC} = 3.6 \times 10^{-4}$; see discussion in Section 2.1). In general, there is good qualitative agreement between the C11 + C15 and the V13 models, the only major difference being

the normalization. The predictions with the linear model with $\xi = 3 \times 10^{-4}$ are nearly identical to the C11 + C15 model, as one would expect from Fig. 3, but here we show the yields for our fiducial choice of $\xi = 9 \times 10^{-4}$. The value at which these N yields flatten off at low Z is reflective of our adopted value of y_N^{CC} (grey dashed line). Up to $\log_{10}(Z/Z_\odot) \approx -0.2$, the KL16+K18 yields predict a similar trend as C11 + C15 and V13, also with a difference in normalization, but at solar and super-solar metallicities they predict much more metallicity-independent N yields than others. The K10 yields, on the other hand, do not agree with any of the other models, instead predicting N yields to *decrease* monotonically with increasing Z. These differences between the K10 and KL16 + K18 models trace back to differences regarding the opacity and mass-loss prescriptions (see discussion in Section 2.2). Although the normalization depends on the SN yields of all elements, we demonstrate in Section 4.2 that reproducing the [N/O]–[O/H] relation as observed requires AGB N yields which scale roughly linearly with metallicity as in the C11 + C15 and V13 models. More specifically, with our adopted O and Fe yields (see discussion at the beginning of Section 2), reproducing the observational constraints that we consider requires *total* N yields (CCSN + AGB) with the metallicity dependence shown by the purple curve in the right-hand panel of Fig. 4.

3 THE MULTIZONE CHEMICAL EVOLUTION MODEL

We use the fiducial model for the Milky Way published by Johnson et al. (2021), which runs using the VICE GCE code (see Appendix A; Johnson & Weinberg 2020; Griffith et al. 2021). Multizone models allow simultaneous calculations of abundances for multiple Galactic regions, making them a more physically realistic option than classical one-zone models for a system like the Milky Way. Furthermore, they can take into account stellar migration in a framework that is much less computationally expensive than hydrodynamical simulations, making them the ideal experiments for our purposes. We provide a brief summary of the model here, but a full breakdown can be found in section 2 of Johnson et al. (2021).

As in previous models for the Milky Way with similar motivations (e.g. Matteucci & Francois [1989]; Schönrich & Binney [2009]; Minchev et al. [2013], [2014]; Minchev et al. [2017]; Sharma et al. [2021]), this model parametrizes the Galaxy disc as a series of concentric rings. With a uniform width of $\delta R_{gal} = 100$ pc, each ring is assigned its own SFH, and with assumptions about outflows and the $\Sigma_{gas} - \dot{\Sigma}_\star$ relation (see discussion below), VICE computes the implied amounts of gas and infall at each time-step automatically. Under the caveat that stellar populations can move and place some of their nucleosynthetic products in rings other than the one they were born in, each ring is otherwise described by a conventional one-zone GCE model. Allowing stars to enrich distributions of radii was a novel addition to this type of model, and Johnson et al. ([2021]) demonstrated that this has a significant impact on enrichment rates from delayed sources such as SNe Ia.

To drive stellar migration, the model makes use of star particles from a hydrodynamical simulation, for which Johnson et al. ([2021]) select the h277 galaxy from the Christensen et al. ([2012]) suite evolved with the *N*-body + SPH code GASOLINE (Wadsley, Stadel & Quinn [2004]); we retain this decision here. h277 spans 13.7 Gyr of evolution, but the sample of star particles with reliable birth radii span 13.2 Gyr in age; the model thus places the onset of star formation ∼500 Myr after the big bang and integrates up to the present day. Previous studies have shown that h277, among other disc galaxies evolved with similar physics, has a realistic rotation curve (Governato et al. [2012]; Christensen et al. [2014a], [b]), stellar mass (Munshi et al. [2013]), metallicity (Christensen et al. [2016]), dwarf satellite population (Zolotov et al. [2012]; Brooks & Zolotov [2014]), H I properties (Brooks et al. [2017]), and stellar age–velocity relation (Bird et al. [2021]). Despite this, there are some interesting differences between h277 and the Milky Way. First and foremost, h277 had only a weak and transient bar and lacks one at the present day, while the Milky Way is known to have a strong, long-lived central bar (e.g., Bovy et al. [2019]). This could indicate that the dynamical history of h277 and its star particles differs significantly from that of the Milky Way. Furthermore, the last major merger in h277 was at a redshift of $z \approx 3$, making it an interesting case study for its quiescent merger history (e.g., Zolotov et al. [2012]), while the Sagitarrius dwarf galaxy is believed to have made pericentric passages around the Milky Way at 1–2-Gyr intervals (Law & Majewski [2010]). Although these differences between h277 and the Milky Way are well understood, their impact on chemical evolution is not. We are unaware of any studies that investigate the impact of different assumptions regarding the Galaxy's dynamical history on predicted abundances; this is, however, an interesting question for future work.

Radial migration of stars proceeds from the h277 star particles in a simple manner; for a stellar population in our model born at a radius R_{birth} and a time t_{birth}, VICE searches for star particles born at $R_{birth} \pm 250$ pc and $t_{birth} \pm 250$ Myr. From the star particles that make this cut, it then randomly selects one to act as that stellar population's *analogue*. The stellar population then assumes the present-day mid-plane distance z and the change in orbital radius ΔR_{gal} of its analogue between its birth and the present day. In the Johnson et al. ([2021]) fiducial model, stellar populations move to their implied final radii with a $\sqrt{\text{age}}$ dependence according to:

$$R_{gal}(T) = R_{birth} + \Delta R_{gal}\sqrt{\frac{t - t_{birth}}{13.2 \text{ Gyr} - t_{birth}}}, \tag{4}$$

where 13.2 Gyr is simply the present day (see discussion above). With displacement proportional to $\sqrt{\text{age}}$, this corresponds to a scenario in

which radial migration proceeds as a diffusion process as modeled by Frankel et al. ([2018], [2019]) and supported by the *N*-body simulations of Brunetti, Chiappini & Pfenniger ([2011]). Although Johnson et al. ([2021]) investigated other assumptions for this time-dependence, in this paper we only use this parametrization (hereafter referred to as the 'diffusion' prescription) and an idealized one in which stars remain at their birth radius until they instantaneously migrate at the present day (hereafter referred to as the 'post-processing' prescription). If VICE does not find any star particles from h277 in its initial $R_{gal} \pm 250$ pc and $t \pm 250$ Myr search, it widens it to $R_{gal} \pm 500$ pc and $t \pm 500$ Myr; if still no candidate analogues are found, VICE maintains the $t \pm 500$ Myr requirement, but assigns the star particle with the smallest difference in birth radius as the analogue. This procedure can be thought of as 'injecting' the dynamics of the h277 galaxy into our multizone chemical evolution model, and it can in principle be repeated for any hydrodynamical simulation of a disc galaxy. As in Johnson et al. ([2021]), we neglect radial gas flows (e.g., Lacey & Fall [1985]; Bilitewski & Schönrich [2012]; Vincenzo & Kobayashi [2020]), instead focusing on the impact of stellar migration.

Rather than using a hydrodynamical simulation, some previous studies have implemented stellar migration using dynamical arguments (e.g. Schönrich & Binney [2009]; Sharma et al. [2021]). An advantage of our approach over this is that these dynamical arguments introduce free parameters which then require fitting to data. It is also unclear to what extent the fit might bias the model into agreement with quantities in the sample not involved in the fit. A disadvantage of our approach is that we are restricted to one realization of our dynamical history; slight variations are not possible. We do not distinguish between 'blurring' and 'churning', terms commonly used to refer to changes in the guiding centre radii of stars and their epicyclic motions, respectively. Both are induced by a variety of physical interactions such as molecular cloud scattering (Mihalas & Binney [1981]; Jenkins & Binney [1990]; Jenkins [1992]), orbital resonances with spiral arms or bars (Sellwood & Binney [2002]; Minchev et al. [2011]), and satellite perturbations (Bird, Kazantzidis & Weinberg [2012]). All of these effects are included in h277 and should therefore be inherited by the stellar populations in our GCE model.

We assume the SFH of the 'inside-out' model from Johnson et al. ([2021]). The time-dependence at a given R_{gal} is described by

$$\dot{\Sigma}_\star \propto (1 - e^{-t/\tau_{rise}})e^{-t/\tau_{sfh}}, \tag{5}$$

where τ_{rise} approximately controls the amount of time the SFR is rising at early times; we set this parameter equal to 2 Gyr at all radii as in Johnson et al. ([2021]). Our e-folding time-scales of τ_{sfh} are taken from a fit of this functional form to the $\Sigma_\star$–age relation in bins of R/R_e for $10^{10.5}$–10^{11} M$_\odot$ Sa/Sb Hubble-type spiral galaxies reported by Sánchez ([2020]). The resulting values of τ_{sfh} are long: ∼15 Gyr at the solar circle ($R_{gal} = 8$ kpc) and as high as ∼40 Gyr in the outer disc (see fig. 3 of Johnson et al. [2021]). This is a consequence of flat nature of the $\Sigma_\star$–age relation reported by Sánchez ([2020]).

Within each $\delta R_{gal} = 100$ pc ring, the normalization of the SFH is set by the total stellar mass of the Milky Way disc and the present-day stellar surface density gradient, assuming that it is unaffected by migration (see appendix B of Johnson et al. [2021]). For the former, we neglect the contribution from the bulge and adopt the total disc stellar mass of 5.17×10^{10} M$_\odot$ from Licquia & Newman ([2015]). For the latter, we adopt a double exponential form describing the thin- and thick-disc components. We take the scale radii of the thin- and thick-discs to be $R_t = 2.5$ and $R_T = 2.0$ kpc, respectively, with

a surface density ratio at $R_{\rm gal} = 0$ of $\Sigma_T/\Sigma_t = 0.27$ based on the findings of Bland-Hawthorn & Gerhard (2016).

Since the Johnson et al. (2021) models run VICE with the SFH specified a priori, determining the gas supply requires an assumption regarding the SFE. Based on the findings of Kennicutt (1998), GCE models often adopt a single power-law relating the surface density of gas $\Sigma_{\rm gas}$ to the surface density of star formation $\dot{\Sigma}_\star$. Recent studies, however, have revealed that the spatially resolved $\Sigma_{\rm gas} - \dot{\Sigma}_\star$ relation is more nuanced than the integrated relation (de los Reyes & Kennicutt 2019; Ellison et al. 2021; Kennicutt & de los Reyes 2021). Some of the uncertainty regarding its details can be traced back to the ongoing debate about the CO-to-H_2 conversion factor (Kennicutt & Evans 2012; Liu, Gao & Greve 2015). Based on a compilation of the Bigiel et al. (2010) and Leroy et al. (2013) data shown in comparison to the theoretically motivated parametrizations of Krumholz et al. (2018, see their fig. 2), Johnson et al. (2021) take a three-component power-law $\dot{\Sigma}_\star \propto \Sigma_{\rm gas}^N$ with index N given by

$$N = \begin{cases} 1.0 & (\Sigma_{\rm gas} \geq 2 \times 10^7 \, {\rm M_\odot \, kpc^{-2}}) \\ 3.6 & (5 \times 10^6 \, {\rm M_\odot \, kpc^{-2}} \leq \Sigma_{\rm gas} \leq 2 \times 10^7 \, {\rm M_\odot kpc^{-2}}) \\ 1.7 & (\Sigma_{\rm gas} \leq 5 \times 10^6 \, {\rm M_\odot \, kpc^{-2}}). \end{cases} \quad (6)$$

The normalization is fixed by setting the SFE time-scale $\tau_\star \equiv \Sigma_{\rm gas}/\dot{\Sigma}_\star$ at surface densities where $N = 1$ to the value derived observationally for molecular gas, denoted by $\tau_{\rm mol}$. This value at the present day is taken to be $\tau_{\rm mol,0} = 2$ Gyr (Leroy et al. 2008, 2013), with a $t^{1/2}$ dependence on cosmic time based on the findings of Tacconi et al. (2018) studying the properties of molecular gas as a function of redshift.

With the yields adopted in the Johnson et al. (2021) models (see discussion at the beginning of Section 2), considerable outflows are required in order to predict empirically plausible abundances. Weinberg et al. (2017) demonstrate analytically that the equilibrium abundance of some element in the gas phase is approximately determined by its yield and the mass loading factor $\eta \equiv \dot{\Sigma}_{\rm out}/\dot{\Sigma}_\star$ with a small correction for the SFH. Johnson et al. (2021) select a scaling of η with $R_{\rm gal}$ such that the equilibrium abundance as a function of radius corresponds to a reasonable metallicity gradient within the Galaxy (see their fig. 3 and discussion in their section 3.1). None the less, yields and the strength of outflows are mutually degenerate parameters since they act as source and sink terms in computing enrichment rates. The absolute scale of nucleosynthetic yields is a topic of debate (see discussion in, e.g. Griffith et al. 2021), and some authors even neglect outflows entirely, arguing that they do not significantly alter the chemical evolution of the Galaxy disc (e.g. Spitoni et al. 2019, 2021). We investigate the impact of simultaneous variations in our yields and the efficiency of outflows in Section 4.2 below and find similar [N/O]–[O/H] relations, suggesting that we would arrive at similar conclusions if we were to neglect outflows and adjust our yields accordingly.

4 RESULTS

In this section, we present the predictions of our GCE models. We establish a fiducial model in Section 4.1, which adopts $y_N^{\rm CC} = 3.6 \times 10^{-4}$ and our linear AGB star yields (equation 3) with $\xi = 9 \times 10^{-4}$ along with the O and Fe yields of Johnson et al. (2021, see discussion in Section 2). We discuss the evolution of this model in radius and time as well as the impact of stellar migration. In Section 4.2, we consider AGB star yield models taken from the literature (see discussion in Section 2.2) and use an empirical [N/O]–[O/H] relation to discriminate among them. For each of these previously published yields, we explore alternate parametrizations of our SN yields and/or

Table 1. A reference on which migration prescription (see Section 3) we take as a default and which AGB star yield model(s) we consider in each section of Section 4. Our linear AGB star yield is defined in equation (3). We use a metallicity-independent IMF-averaged massive star yield of $y_N^{\rm CC} = 3.6 \times 10^{-4}$ throughout, exploring alternate, metallicity-dependent parametrizations in Section 4.2.2 only (right-hand panel of Fig. 6). We do not present multizone GCE models in Sections 4.2.3 and 4.6.

Section	AGB star yield model(s)	Migration prescription
4.1	Linear	Diffusion
4.2	C11+C15, V13, K10, KL16 + K18	Post-processing
4.2.1	Linear, C11 + C15, V13	Post-processing
4.2.2	K10, KL16 + K18	Post-processing
4.2.3	N/A	N/A
4.3	Linear	Post-processing
4.4	Linear	Diffusion
4.5	Linear	Diffusion
4.6	N/A	N/A

the efficiency of outflows which may address their shortcomings in reproducing the observed trend. We return to the fiducial model in Section 4.3 to demonstrate the dominance of the metallicity dependence of N yields over the AGB star DTD in establishing the gas-phase [N/O]–[O/H] relation. To make the comparisons more clear, we make use of the post-processing migration prescription in Sections 4.2 and 4.3 but otherwise retain the diffusion prescription (see discussion in Section 3). In Section 4.4, we compare our fiducial [N/O] versus age and [N/O] versus [O/Fe] trends to the stellar abundances derived from APOGEE data by Vincenzo et al. (2021a). In Section 4.5, we demonstrate how variations in the SFE or inflow rate can induce scatter in the gas-phase [N/O]–[O/H] relation. We finish presenting our results in Section 4.6 by offering an analytic understanding of the [N/O]–[O/H] relation obtained with chemical equilibrium arguments inspired by Weinberg et al. (2017). As a reference for the reader, in Table 1 we provide a summary of which migration prescriptions we take as a default and which AGB star yield models we consider in each subsequent subsection.

4.1 Evolution of a fiducial model

In the left-hand panel of Fig. 5, we plot the evolution of N and O abundances in the gas phase at five different Galactocentric radii in our fiducial model (see paragraph above). At early times, [O/H] is low and [N/O] reflects the ratio of the CCSN yields ([N/O]$_{\rm cc} \approx -0.7$). Consequently, the tracks in each ring are similar. Once lower mass stars begin to evolve through an AGB phase, they enrich the ISM with N but negligible amounts of O, increasing [N/O]. At this point, the tracks in each ring separate from one another. This separation is a consequence of the metallicity gradient in [O/H] being established early in the Galaxy's evolution. The radial gradient in our model arises out of a decrease in the equilibrium abundance of O with increasing radius. Produced on short time-scales by CCSNe, O achieves equilibrium faster than elements produced by delayed nucleosynthetic sources (Weinberg et al. 2017). The ISM therefore reaches equilibrium in O soon after AGB stars begin producing N, after which [N/O] continues to increase at an approximately fixed [O/H] at all radii (see also Fig. 8 and associated discussion in Section 4.4). The separation of these evolutionary tracks contests the popular interpretation that the [N/O]–[O/H] relation arises as an evolutionary sequence, instead suggesting a superposition of evolutionary endpoints at equilibrium values set by different outflow efficiencies (a similar argument was made by Chiappini et al.
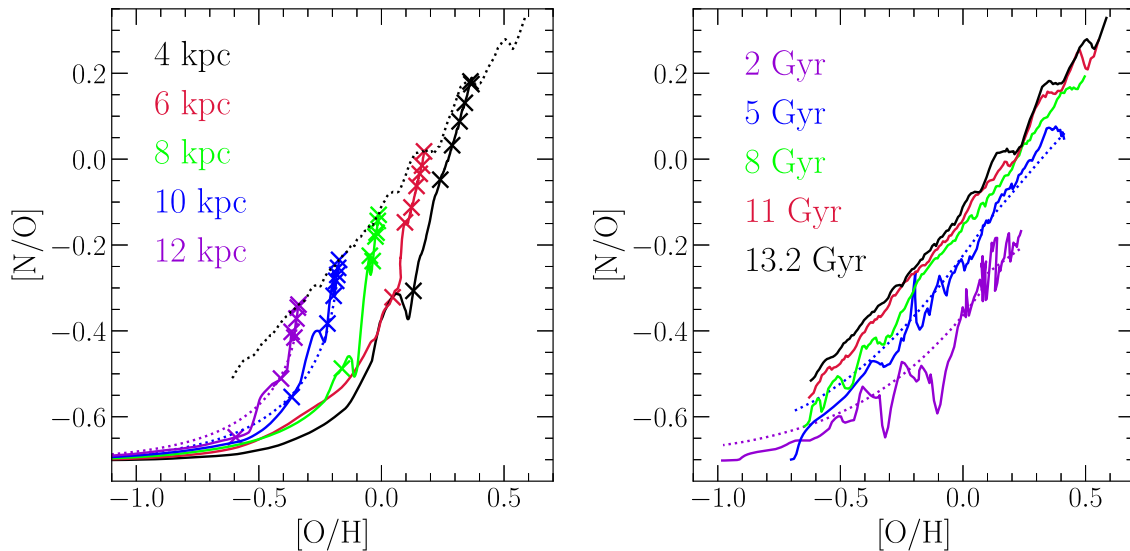
Figure 5. Left: The gas-phase [N/O]–[O/H] relation parametrized by time at fixed radius (solid coloured lines) in the fiducial model. X's denote the abundances at $t = 2, 4, 6, 8, 10, 12$, and 13.2 Gyr (the present day) at all radii. The dotted black line is the same as the solid black line in the right-hand panel. Coloured dotted lines mark the evolution of our model at $R_{gal} = 10$ and 12 kpc when we neglect the impact of stellar migration on enrichment rates (i.e., the 'post-processing' migration prescription from Johnson et al. 2021; see discussion in Section 3). Right: The gas-phase [N/O]–[O/H] relation parametrized by radius at various snapshots (solid coloured lines) in our fiducial model. Similar to the left-hand panel, coloured dotted lines denote the resulting relation at $t = 2$ and 5 Gyr when we neglect stellar migration in computing enrichment rates.

2003). Similar arguments have been made regarding low [α/Fe] disc stars (e.g. Schönrich & Binney 2009; Nidever et al. 2014; Buck 2020; Sharma et al. 2021). In short, a given ring in our model does not evolve along the [N/O]–[O/H] relation, instead following this 'rightward-then-upward' trajectory dictated by the time-scales on which N and O achieve equilibrium.

Because there is a delay between a stellar population's formation and N production from its AGB stars ($\sim$250 Myr in this model; see Fig. 4), stellar migration can in principle occur within this time interval. Although the bulk of migration occurs on longer time-scales, this characteristic delay is comparable to the dynamical time of the Milky Way and is thus adequate for kinematic heating to at least begin. In zoom-in hydrodynamical simulations from the FIRE[10] suite (Hopkins et al. 2014), El-Badry et al. (2016) find that stars in a $M_\star \approx 10^{10.6}$ M$_\odot$ galaxy can migrate 1–2 kpc within 1 Gyr of their formation. Consequently, N enrichment rates at fixed R_{gal} may differ significantly from their expected values given the SFH at that radius because stellar migration induced a deficit or surplus of N-producing AGB stars. These tracks can thus move vertically in the [N/O]–[O/H] plane in response to AGB stars moving between rings as the Galaxy evolves, producing the 'jitter' in these evolutionary tracks. We demonstrate this effect by comparing the solid blue and purple lines to their dotted counterparts. These are the tracks we compute using the post-processing migration prescription which eliminates the impact of migration on enrichment rates (see discussion in Section 3).

In the right-hand panel of Fig. 5, we plot the gas-phase [N/O]–[O/H] relation predicted by the model at various snapshots. To obtain this, we simply take the N and O abundances in the ISM at a given output time for each $\delta R_{gal} = 100$ pc ring at $R_{gal} > 2$ kpc and plot them as a line. The relation is generally time-independent at $t \gtrsim 5$ Gyr. Although there is some slight evolution toward higher [N/O], the total change in [N/O] over this time

interval is well within the intrinsic scatter derived observationally (see Fig. 1). Even at $t = 2$ Gyr, corresponding to $z \approx 2.6$, [N/O] at fixed [O/H] is only $\sim$0.2 dex lower than its value at the present day. Especially when considering the intrinsic scatter that would arise if we were to consider models with, e.g. different SFHs, this calculation supports previous arguments that the redshift evolution of the [N/O]–[O/H] relation is minimal (Vincenzo & Kobayashi 2018; Hayden-Pawson et al. 2022).

We again demonstrate the impact of stellar migration in the right-hand panel of Fig. 5 by comparing the blue and purple solid lines to their dotted counterparts, which quantify the relation using the post-processing migration prescription. This indicates that the local jitter seen in the relation at a given time is a consequence of migration as discussed above. The mechanism by which stellar migration imposes these features in the [N/O]–[O/H] plane is qualitatively similar to what Johnson et al. (2021) find for SN Ia production of Fe. They found that the SN Ia rate in this model can vary by as much as a factor of $\sim$3 at large radii ($R_{gal} \gtrsim 9$ kpc). When a deficit or surplus of SN Ia events is sustained for timescales comparable to the depletion time of the local ISM, the gas-phase abundance of Fe increases or decreases accordingly. As a consequence, some of the stellar populations that form during these events are Fe-poor enough to present as young stars ($\lesssim$6 Gyr) with significantly super-solar [α/Fe] ratios, some of which are indeed observed in the solar neighbourhood with APOGEE[11] (Chiappini et al. 2015; Martig et al. 2015, 2016; Warfield et al. 2021). In the case of N, the effect is smaller ($\lesssim$0.1 dex in [N/O]) because our model predicts N yields to be ejected from stellar populations $\sim$5 times faster than Fe (Fig. 4). Consequently,

---

[10]https://fire.northwestern.edu

[11]Although some of these stars appear to have mis-labelled ages (Jofré et al. 2016; Yong et al. 2016; Izzard et al. 2018; Silva Aguirre et al. 2018; Miglio et al. 2021), this phenomenon could explain an intrinsically young sub-component (Hekker & Johnson 2019; see discussion in sections 3.1 and 3.4 of Johnson et al. 2021).

there is less time for stellar migration to occur within the time-scale of N production than there is within the time-scale of Fe production.

To assess how well our model characterizes N production in the Milky Way and external galaxies, in the next section we compare the present-day [N/O]–[O/H] relation (solid black line in the right-hand panel of Fig. 5) to the Dopita et al. (2016) trend. We do the same for our AGB yield models taken from the literature (see discussion in Section 2.2), exploring variations of other model parameters which may address their shortcomings. We then return to our fiducial model thereafter for additional tests against observed data.

4.2 Comparison to observed gas-phase trends

We use the Dopita et al. (2016) [N/O]–[O/H] relation, which is inferred by fitting local stars and H II regions spanning a wide range of [O/H], as our observational benchmark. As seen in Fig. 1, the Pilyugin et al. (2010) 'ONS' calibration leads to a steeper relation at high [O/H]. Following Vincenzo et al. (2021a), we adopt the Dopita et al. (2016) relation because it agrees well with the trends found for APOGEE disc stars and with results for MaNGA galaxies (Belfiore et al. 2017, see Fig. 1). None the less, uncertainties in the observed trends remain, and adopting a significantly different relation would lead to different conclusions about the metallicity dependence of N yields. To make the comparison between different yield models more clear, we neglect the impact of stellar migration on enrichment rates and make use of the post-processing migration prescription in this section (see discussion in Section 3). In each panel of Fig. 6, black points show the Dopita et al. (2016) trend. The purple curve in the middle panel shows the prediction of our fiducial (linear) yield model, which achieves excellent agreement with this observational benchmark.

In the left-hand panel of Fig. 6, we compare our model predictions with each of the AGB star yield tables predicted from stellar evolution models (see Fig. 3 and discussion in Section 2.2). Swapping our linear yields (equation 3) out from the fiducial model for any of these AGB yields taken from the literature results in a failure to reproduce the observed [N/O]–[O/H] relation. The C11 + C15 and V13 yields are able to reproduce the qualitative trend, but with an incorrect normalization. The K10 and KL16 + K18 yields, on the other hand, fail to reproduce the steadily sloped increase of [N/O] with [O/H]. The inverse dependence of [N/O] with [O/H] predicted by the K10 AGB star yields can be understood by the interaction between TDU and HBB (see discussion in Section 2.2). Both effects are stronger at low metallicity, and since all of the K10 stars experiencing HBB also experience TDU (see their table 1), such a result is unsurprising. This overlap also occurs in the KL16 + K18 models, but their yields predict a relatively flat [N/O]–[O/H] relation because of updated model inputs regarding opacity and mass loss and the impact this has on ^{14}N yields (see discussion in Section 2.2).

4.2.1 Variations in SN yields and outflows

In order to successfully reproduce the observations with the C11 + C15 and V13 yields but without adjusting the GCE model parameters, we find that we must artificially amplify them by factors of ∼3 and ∼2, respectively. We illustrate the results of these modified yield models and for our fiducial linear model with a normalization of $\xi = 9 \times 10^{-4}$ in the middle panel of Fig. 6. Although the V13 model predicts an [N/O]–[O/H] relation that is slightly shallower than the Dopita et al. (2016) data, the predictions are reasonably within the scatter seen in Fig. 1.

As foreshadowed in Section 2, we can reproduce the [N/O]–[O/H] relation if we alternatively use the unmodified C11 + C15 and V13 yields and make simultaneous adjustments to the strength of outflows and the normalization of our SN yields. We cannot modify one without modifying the other, because the Johnson et al. (2021) model sets the Galactic [O/H] gradient according to a scaling of the equilibrium abundance with radius via an increase in the strength of outflows. Adjustments to the strength of outflows must therefore be accompanied by a revision of all SN yields with a similar multiplicative factor. The central panel of Fig. 6 shows a model that uses the unmodified C11 + C15 yields and $y_O^{CC} = 0.005$ with the outflow mass-loading factor lowered by a factor of three. We also show a variation with $y_O^{CC} = 0.01$, the C11 + C15 yields amplified by a factor of two, and the strength of outflows adjusted accordingly. While each of these variations lie along the observed [N/O]–[O/H] relation, they span slightly different ranges in [O/H] because the relation between yields and outflows in determining the equilibrium abundance is not exactly one-to-one.[12] Regardless of the assumed normalization, we find that the observed [N/O]–[O/H] relation can be reproduced as long as the metallicity-dependence of population-averaged AGB N yields is approximately linear. We expect that these results will hold if outflows are omitted since this corresponds to the limiting case in which we would scale our yields down by larger factors.

Lowering our SN yields by a factor of 2–3 is plausible if a substantial fraction of massive stars collapse directly to black holes as opposed to exploding as SNe at the ends of their lives. Our IMF-averaged massive star yields (see discussion in Section 2.1) are based on a Kroupa (2001) IMF combined with SN nucleosynthesis models in which most $M > 8$ M$_\odot$ stars explode as a CCSN (e.g. Woosley & Weaver 1995; Chieffi & Limongi 2004, 2013; Nomoto et al. 2013; Limongi & Chieffi 2018). However, many massive stars may collapse to form black holes without a SN (Gerke, Kochanek & Stanek 2015; Pejcha & Thompson 2015; Ertl et al. 2016; Sukhbold et al. 2016; Adams et al. 2017; Basinger et al. 2021; Neustadt et al. 2021). With the explosion landscape predicted by their W18 neutrino-driven engine, the CCSN models of Sukhbold et al. (2016) predict $y_O^{CC} = 0.0056$ (Griffith et al. 2021), nearly three times lower than our fiducial value.[13] Extensive black hole formation would also lower y_{Fe}^{CC}, and a lower normalization of y_{Fe}^{Ia} may be compatible with observational constraints on SN Ia rates (see discussion in Section 2).

Another alternative is to retain high y_O^{CC} but assume that Galactic winds preferentially remove SN products relative to AGB products. In particular, Vincenzo et al. (2016a) are able to reproduce the [N/O]–[O/H] relation in chemical evolution models with the V13 yields by implementing a differential wind in which outflows remove O but not N from the star forming gas reservoir. We find similar results for the V13 yields if we simply add a portion of the SN products (both CCSN and SN Ia) directly to the outflow, which is otherwise composed of swept up ambient ISM with the same abundance ratios but reduced η. If SNe are the sources of outflow-driving winds but AGB stars do not significantly contribute, it would be reasonable to expect some portion of the SN ejecta to be swept up by the wind; recent theoretical (Christensen et al. 2018) and observational

---

[12]Rather, it is one-to-one with $1 + \eta - r$, where η is the mass-loading factor and $r \approx 0.4$ is a corrective term for recycling (Weinberg et al. 2017).
[13]This can be calculated with VICE using the `vice.yields.ccsne.fractional` function, designed to compute values of y_X^{CC} for various elements under a variety of assumptions.
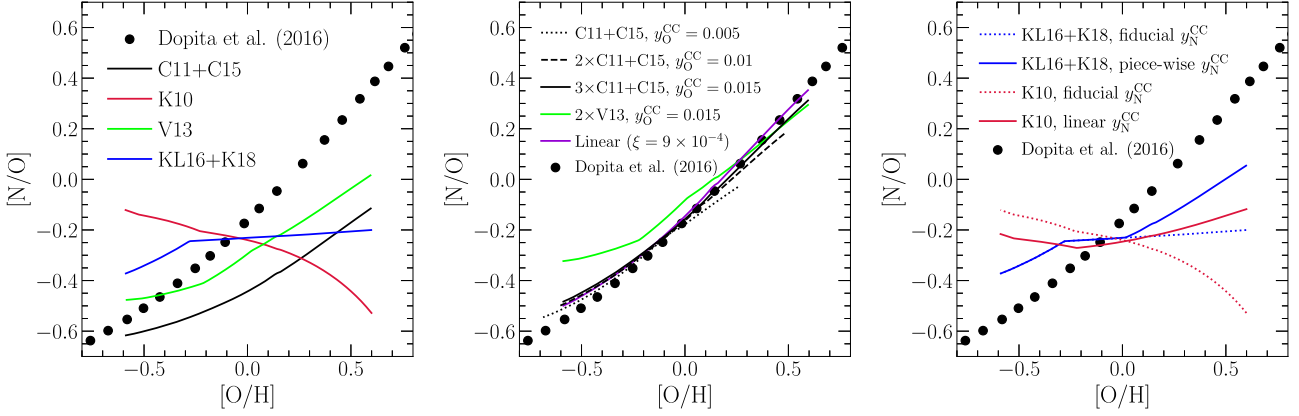
Figure 6. Left: The present-day gas-phase [N/O]–[O/H] relation predicted by our model with each of the four AGB star yield tables predict by stellar evolution models discussed in Section 2.2, colour coded according to the legend. We include the Dopita et al. (2016) empirical relation as the observational benchmark. Middle: The same as the left-hand panel, but for a case where we artificially amplify the C11 + C15 yields by a factor of 3 and the V13 yields by a factor of 2. We show our fiducial model using the linear AGB star yields with a slope of $\xi = 9 \times 10^{-4}$ in a solid purple line. The black dashed and dotted lines show additional models in which we vary the normalization of the C11 + C15 yields, our SN yields, and the outflow mass loading factor simultaneously (see discussion in Section 4.2.1). Right: The same as the left-hand panel, but comparing the predictions made by the K10 and KL16 + K18 yields with our fiducial value of y_N^{CC} (dotted lines, same as left-hand panel) to those with alternate forms of y_N^{CC} (solid lines; see equations 7 and 8 and discussion in Section 4.2). We show all predictions with our post-processing migration prescription (see discussion in Section 3).

arguments (Chisholm, Tremonti & Leitherer 2018) indeed suggest such a scenario.

4.2.2 Metallicity-dependent CCSN yields of N

While the issue for the C11 + C15 and V13 yields is one of normalization, our models with the K10 or KL16 + K18 AGB yields predict a qualitatively incorrect trend of [N/O] with [O/H]. This discrepancy cannot be repaired by changing y_O^{CC}. However, the N yield is the sum of CCSN and AGB star contributions, so it is reasonable to ask if plausible changes to the metallicity dependence of the CCSN yield can compensate. Motivated by the observed [N/O] plateau at low metallicity and by the predictions of rotating massive star models, we have thus far assumed a metallicity-independent $y_N^{CC} = 3.6 \times 10^{-4}$. However, the non-rotating CCSN models of Nomoto et al. (2013) suggest that y_N^{CC} may increase at super-solar metallicity (see Fig. 3). We therefore construct the following parametrization for use with the KL16 + K18 AGB star yields:

$$y_N^{CC} = (3.6 \times 10^{-4}) \max\left(1, \frac{Z}{Z_\odot}\right). \tag{7}$$

Using this yield combination in our GCE model produces the blue solid curve in the right-hand panel of Fig. 6. While agreement with the Dopita et al. (2016) trend is somewhat improved, this model is still far from the empirical [N/O]–[O/H] relation. Achieving agreement while using the KL16 + K18 yields would require still higher CCSN yields at $Z > Z_\odot$ and somewhat lower CCSN yields at $Z < Z_\odot$.

Because the K10 AGB model predicts a high N yield at low metallicity (Fig. 4), we combine it with the predicted yields of the non-rotating CCSN models from Limongi & Chieffi (2018), which we approximate as

$$y_N^{CC} = (3.6 \times 10^{-4})\left(\frac{Z}{Z_\odot}\right) \tag{8}$$

(diagonal dotted line in Fig. 2, left). This combination produces the red solid line in the right-hand panel of Fig. 6. Although the discrepancy with the Dopita et al. (2016) trend is somewhat reduced, this

model still underpredicts [N/O] at $Z > Z_\odot$ and overpredicts [N/O] at $Z < Z_\odot$ by large margins.

We conclude that the metallicity dependence of N yields predicted by the KL16 + K18 and, especially, K10 AGB models are empirically untenable unless massive star yields are far from theoretical expectations. The implications for stellar astrophysics are uncertain, but inspection of Fig. 3 suggests that the problem of these AGB star models originates in the coexistence of TDU and HBB over a substantial mass range ($M \gtrsim 4\ M_\odot$): in both models, every star that experiences HBB also experiences TDU.

4.2.3 Summary

The gas-phase [N/O]–[O/H] relation in the Milky Way disc predicted by our GCE model agrees well with the Dopita et al. (2016) trend characterizing local stars and H II regions if we assume a metallicity-independent $y_N^{CC} = 3.6 \times 10^{-4}$ as suggested by rotating massive star models (Limongi & Chieffi 2018) and the linear model of AGB yields in equation (3) with $\xi = 9 \times 10^{-4}$. Reproducing the empirical trend with the C11 + C15 (V13) AGB yields requires renormalizing those yields by a factor of 3 (2) or, alternatively, lowering the assumed CCSN O yield y_O^{CC} and N yield y_N^{CC} by the same factor. Lowering y_O^{CC} could be physically justified if a large fraction of massive stars collapse to black holes without producing CCSNe, and it may be empirically tenable in a model where y_{Fe}^{CC}, y_{Fe}^{Ia}, and outflow mass loading efficiencies η are all lowered by a similar factor. The metallicity dependence of AGB star yields predicted by the K10 or KL16 + K18 models, flat or even declining with increasing metallicity, is difficult to reconcile with the observed [N/O]–[O/H] trend.

4.3 Metallicity dependence versus age dependence

Despite predicting a different mass dependence for Y_N^{AGB} (see Fig. 3), the renormalized C11 + C15 and V13 yields both reproduce the [N/O]–[O/H] relation reasonably well. This result suggests that the metallicity dependence plays a much more important role than the DTD in establishing this correlation. To investigate this

point further, we consider two variants of our fiducial model: one with the dependence on stellar age (or, equivalently, stellar mass) removed from the enrichment rate calculations, and the other with the metallicity dependence removed. We return to our linear AGB yield model with $\xi = 9 \times 10^{-4}$, and to make this comparison more straightforward, we use the post-processing migration model (see discussion in Section 3).

To remove the age dependence, we simply eject the AGB star yields alongside the CCSN yield instantaneously after a single stellar population forms. We pre-compute the N yields from all AGB stars associated with a 13.2 Gyr old stellar population as a function of progenitor metallicity in a similar fashion as in the right-hand panel of Fig. 4. Since VICE works from IMF-averaged CCSN yields assumed to be injected instantaneously following a single stellar population's formation (see discussion in Section 2.1), we make use of the software's capability to let the user specify functional forms for nucleosynthetic yields and simply add this N yield to y_N^{CC} and set Y_N^{AGB} to zero. In this model, y_N^{CC} inherits a metallicity dependence from the AGB star yields and has the exact shape of the purple curve in the right-hand panel of Fig. 4. To remove the metallicity dependence, the procedure is much simpler: we simply evaluate Y_N^{AGB} at our assumed solar metallicity of $Z_\odot = 0.014$ at all time-steps regardless of that which is predicted for a stellar population. In this variation, AGB star production still occurs on a DTD inherited from the stellar mass–lifetime relation (Larson 1974) and the mass dependence of the linear yield model.

We illustrate these predictions in Fig. 7. The [N/O]–[O/H] relation from the model with no age dependence is nearly identical to the prediction found in our fiducial model, while the prediction with no metallicity dependence is considerably different. This result is rather unsurprising given the short characteristic time-scales of N production ($\sim$250 Myr, see the middle panel of Fig. 4). Mathematically, there is little difference in the enrichment rates if all of a stellar population's N is produced immediately as opposed to from a prompt, sharply declining DTD. The metallicity dependence, however, is paramount to the [N/O]–[O/H] relation, which is expected given the results in Fig. 3 and consistent with previous arguments that the increase in [N/O] at high [O/H] is a consequence of secondary N production (Vila-Costas & Edmunds 1993; van Zee et al. 1998; Henry & Worthey 1999; Pérez-Montero & Contini 2009; Berg et al. 2012; Pilyugin et al. 2012; Andrews & Martini 2013; Hayden-Pawson et al. 2022). Fig. 7 implies that the gas-phase [N/O]–[O/H] relation offers little if any constraining power over the mass dependence of N yields from AGB stars.

4.4 Comparison to stellar abundances in the Milky Way disc

Although N abundances are typically measured in the gas-phase in external galaxies, APOGEE (Majewski et al. 2017) has measured N abundances in large stellar samples spanning many regions of the Milky Way. By additionally making use of these data, we can investigate trends with stellar age and [O/Fe] at fixed metallicity. Before comparing the predictions of GCE models to N abundances derived from spectra of red giant samples such as APOGEE, it is essential to adjust the measurements for internal processes known to alter the surface compositions of stars because GCE models predict the birth abundances. During the main sequence lifetime of $M \gtrsim 1.3\,M_\odot$ stars, the CNO cycle processes much of the C and O nuclei in the core into ^{14}N. When the star evolves off the main sequence, this N-rich material is mixed with the outer convective layers, increasing the N abundance in the photosphere (Gilroy 1989; Korn et al. 2007; Lind et al. 2008; Souto et al. 2018, 2019). Using MESA
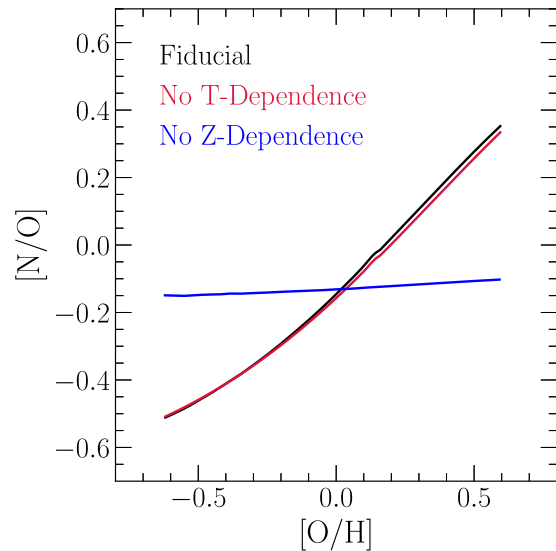

Figure 7. A comparison between our fiducial model with post-processing migration (black) and variations with the time dependence (red) and metallicity dependence removed (blue). To remove the time dependence, we pre-compute the AGB star yields of N from 13.2 Gyr old stellar populations as a function of metallicity as in the right-hand panel of Fig. 4, then incorporate this into the prompt CCSN yields and set the delayed AGB star contribution to zero. To remove the metallicity dependence, we evaluate the yields at our assumed solar metallicity of $Z_\odot = 0.014$ at all time-steps.

stellar evolution models (Paxton et al. 2011, 2013, 2015, 2018) with standard mixing prescriptions, Vincenzo et al. (2021a) developed a recipe to approximate the birth abundances of C, N, and O and applied it to the sample of APOGEE/Kepler red giants with asteroseismic mass measurements from Miglio et al. (2021). They found good agreement between the mean trend of [N/O] with [O/H] for APOGEE disc stars and the Dopita et al. (2016) trend. Since our fiducial model reproduces the Dopita et al. (2016) trend over most of its history (Fig. 5), it should also reproduce the [N/O]–[O/H] relation for APOGEE disc stars.

Our models predict a correlation between N and Fe abundances in the gas-phase which turns out to be important to understanding how the model predictions compare to stellar abundances. In Fig. 8, we plot the evolution of [N/H], [O/H], and [Fe/H] in the ISM at $R_{gal} = 4$, 8, and 12 kpc in our fiducial model with linear AGB yields (equation 3) and the diffusion migration prescription (see discussion in Section 3). [N/H] is more correlated with [Fe/H] than [O/H] at all radii, and the relation persists up to look-back times of $\sim$10 Gyr. This arises in part because N and Fe are both produced in significant quantities by delayed enrichment sources while O is produced almost entirely on short time-scales by CCSNe (see discussion in Section 2). Although the production time-scale of N from single stellar populations is short (see discussion in Section 2.3), metallicity dependent yields require more abundant species such as O to be produced and reach an equilibrium before N yields stabilize. When many stellar populations are present, the bulk of the N production will thus always follow the bulk production of more abundant species; this is qualitatively similar to what Johnson & Weinberg (2020) found regarding the production timescales of Sr and Fe (see also Tinsley 1979). As a consequence of both its slight delay and its metallicity-dependent yields, N reaches its equilibrium abundance on time-scales similar to Fe rather than O. Due to the prompt and metallicity
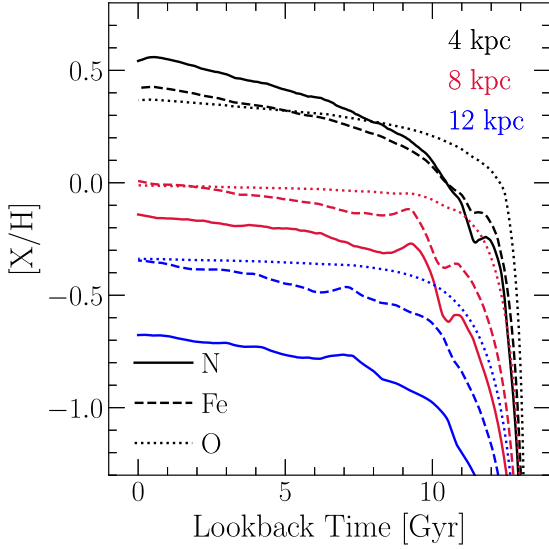
Figure 8. [N/H] (solid), [Fe/H] (dashed), and [O/H] (dotted) in the gas-phase as a function of look-back time in the fiducial model at $R_{\rm gal} = 4$ (black), 8 (red), and 12 kpc (blue).

independent nature of O enrichment, [O/H] is near equilibrium as far back as ∼10 Gyr ago while [N/H] and [Fe/H] are not.

Combining the Vincenzo et al. (2021a) [N/O] ratios with the APOGEE stellar ages taken from Miglio et al. (2021), we illustrate the [N/O]–age relation in bins of [Fe/H] as predicted by our model and measured by APOGEE in the left-hand panel of Fig. 9. In good agreement with the observational measurements, the model predicts the [N/O]–age relation to be relatively flat in bins of [Fe/H]. This arises as a consequence of the N–Fe correlation and the fast approach to equilibrium in [O/H] as discussed above (see Fig. 8). A bin in [Fe/H] approximately corresponds to a bin in [N/H], and by extension a bin in [N/O] as well since [O/H] is nearly constant at fixed radius up to ∼10 Gyr ago.

In the right-hand panel of Fig. 9, we compare our model predictions to the [N/O]–[O/Fe] relation at fixed [O/H] reported by Vincenzo et al. (2021a). The model correctly predicts a significant inverse relationship between [N/O] and [O/Fe]. This is again a consequence of the N–Fe correlation demonstrated in Fig. 8: [N/H] increases with [Fe/H], so at fixed [O/H], [N/O] increases as [O/Fe] decreases. This is another important success of our model. Vincenzo et al. (2021a) demonstrate that high [α/Fe] and low [α/Fe] disc populations show a dichotomy in [N/O]. The Johnson et al. (2021) GCE model produces a broad but continuous [α/Fe] distribution rather than the bimodal distribution found in previous works (e.g., Hayden et al. 2015; Vincenzo et al. 2021b), but Fig. 9 suggests that a model tuned to produce the [α/Fe] bimodality would also produce a dichotomy in [N/O].

Quantitatively, our model slightly underpredicts [N/O] in the lower metallicity bins in both panels of Fig. 9. In general, our model occupies a noticeably wider range in [N/O] than do the Vincenzo et al. (2021a) measurements at all ages and all [O/Fe]. This could be a sign that the AGB star yields of N in our fiducial model scale slightly too strongly with the total metallicity Z. Since our fiducial model assumes an exactly linear scaling of the N yield with Z (see equation 3), this suggests that perhaps a slightly sub-linear scaling would be more accurate, but only barely because the discrepancies in Fig. 9 are at the ∼0.1 dex level.

Although we demonstrate in Section 4.3 that the metallicity dependence of the yield plays the strongest role in establishing the [N/O]–[O/H] relation, the DTD plays a significant role in shaping the stellar abundances. In the model in which AGB nucleosynthetic yields are injected instantaneously along with CCSN products, the N–Fe correlation described above is no longer present. Instead, N approaches equilibrium on much faster time-scales, resulting in it being much more correlated with O than Fe, and the resulting [N/O]–age relation is positively sloped at fixed [Fe/H]. This suggests that the DTD may play a minimal role in establishing gas-phase abundances but is important in shaping stellar abundances. We find additional discrepancies if we instead attribute the delayed N production to a metallicity-dependent SN Ia yield with the same $t^{-1.1}$ DTD that we adopt for Fe. The agreement in Fig. 9 suggests that our fiducial model has a fairly accurate separation of CCSN and AGB contributions and that the ∼250 Myr characteristic delay for AGB enrichment predicted by this model is approximately correct – instantaneous N enrichment is too fast and $t^{-1.1}$ enrichment is too slow to match the observations.

4.5 The sources of scatter in the [N/O]–[O/H] relation

Schaefer et al. (2020) demonstrate that intrinsic scatter in the gas-phase [N/O]–[O/H] relation is correlated with variations in the local SFE. This is expected from one-zone GCE models (e.g., Mollá et al. 2006; Vincenzo et al. 2016a). Although we have demonstrated in Section 4.1 that the impact of stellar migration on enrichment rates is small, it could none the less contribute additional scatter in the observed [N/O]–[O/H] relation. Our models, taking into account the effects of migration on the enrichment rates while allowing full control over the SFH and the SFE through VICE, are an ideal tool with which to address this question.

To this end, we construct two variants of our fiducial model with linear AGB yields (equation 3) and the diffusion migration prescription (see discussion in Section 3). While the fiducial model specifies the SFH *a priori* and lets VICE compute the infall history $\dot{\Sigma}_{\rm in}$, here we specify the infall history as a function of radius and time. As we will demonstrate below, the effects of dilution play an important role in driving variations in the [N/O]–[O/H] plane in these variants, and by specifying the infall history we have more control over the amount of dilution. In a similar fashion as in our fiducial model, we normalize $\dot{\Sigma}_{\rm in}$ such that a stellar mass consistent with that reported by Licquia & Newman (2015) arises from the simulation. All other evolutionary parameters are the same as described in Section 3.

In the first variant, the SFE exhibits 50 per cent sinusoidal oscillations with time over 2-Gyr periods:

$$\tau_\star(R_{\rm gal}, t) = \tau_{\star,\rm J21}(R_{\rm gal}, t) \left(1 + 0.5 \sin \left(\frac{2\pi t}{2\,{\rm Gyr}} \right) \right). \quad (9)$$

The infall rate is constant in each ring with a value determined by normalizing to the present day stellar mass and stellar surface density gradient of the Milky Way. Our choice of a 50 per cent amplitude is comparable to the observationally derived scatter in molecular gas depletion times according to multiple measurement methods (see figs 4 and 5 of Tacconi et al. 2018 and references therein). Furthermore, variations in the SFE are of similar magnitude in h277, the galaxy from which our model's migration history is drawn. In the second variant, the SFE is constant and the infall rate oscillates with a 75 per cent amplitude about its value in the first variant:

$$\dot{\Sigma}_{\rm in}(R_{\rm gal}, t) = \langle \dot{\Sigma}_{\rm in} \rangle \left(1 + 0.75 \sin \left(\frac{2\pi t}{2\,{\rm Gyr}} \right) \right). \quad (10)$$
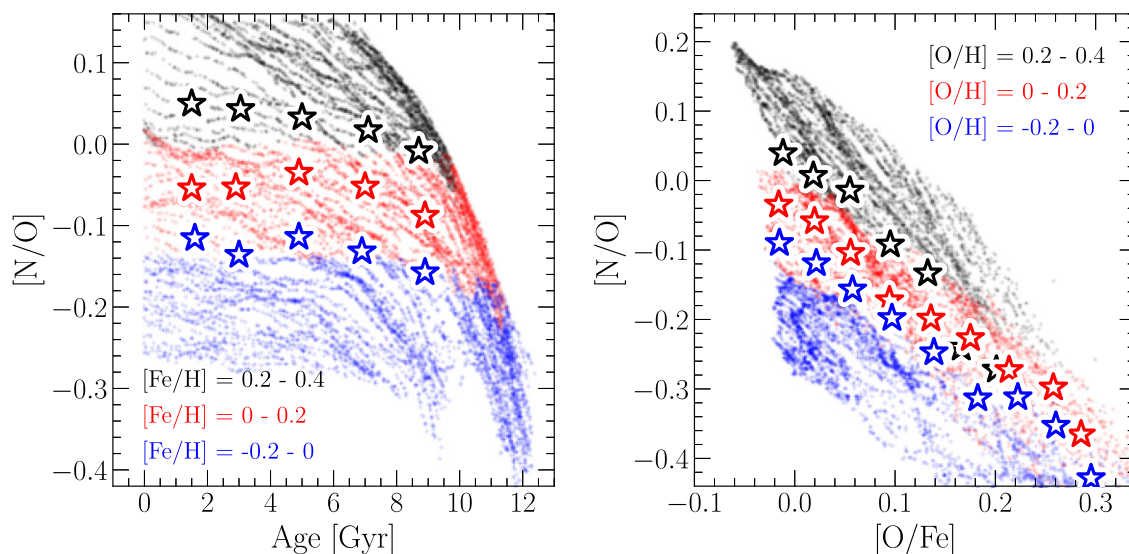
Figure 9. Left: [N/O] as a function of stellar age for 5000 stars randomly sampled from our model stellar populations in three bins of [Fe/H] (coloured points). Stars quantify the median trend in [N/O] with age using N abundances corrected for internal mixing processes reported by Vincenzo et al. (2021a) in the same bins of [Fe/H]. Right: The same as the left-hand panel, but instead showing [N/O] as a function of [O/Fe] in bins of [O/H].

The amplitude of 75 per cent is chosen such that the ensuing variability in the SFR is of similar magnitude between the two models (∼40 per cent). We additionally run a model in which neither the accretion rate nor the SFE oscillate, replacing the fiducial model used in previous sections with this constant infall model. Otherwise, the evolutionary differences beyond simple oscillations complicate the comparison.

These variant models characterize evolutionary pathways in which star formation is more episodic than previously explored. In a real galaxy, variability in the SFE and the SFR is likely non-sinusoidal and not with constant amplitude. A sample of galaxies will have different amplitudes and be seen at different phases in their variability, and the impact of this on their N and O abundances will present as intrinsic scatter in a sufficiently large sample. By comparing models with and without reasonable amounts of variability in these quantities while taking into account radial migration, we can assess which quantities impact abundances more strongly and are thus the more likely causes of intrinsic scatter in the observed [N/O]–[O/H] relation.

In the left-hand panel of Fig. 10, we plot the predicted gas-phase [N/O]–[O/H] relation for five snapshots covering one cycle of fluctuations induced by variability in $\tau_\star$ according to equation (9). This model predicts an ∼0.1 dex dynamic range in [N/O] at fixed [O/H], whereas the constant model with no variability in $\tau_\star$ predicts the relation to be quite steady over this time interval. This suggests that stellar migration, present in both the constant model and this oscillatory variant, does not induce significant variability in the [N/O]–[O/H] plane; however, we demonstrate below that its effects are none the less non-negligible. The minimal impact of stellar migration traces back to the timescales of N production from single stellar populations (see Fig. 4 and discussion in Section 2.3): with most N production occurring within ∼250 Myr of a stellar population's formation, most stars will not migrate far from their birth radius by the time they produce most of their N, and the resulting impact on abundances is small.

The behavior in the [N/O]–[O/H] plane predicted by the oscillatory SFE variant is driven by the tug-of-war between dilution and re-enrichment associated with oscillations in $\tau_\star$. When star formation quickens, O production increases in proportion. The ISM abundance

and consequently the N yields increase as well. Because of the slight but none the less finite delay-time of its production by AGB stars, the N enrichment rate lags slightly behind O. [N/O] therefore decreases, and the ISM moves down and to the right in the [N/O]–[O/H] plane. When star formation eventually slows, O production again follows suit. The N enrichment rate, as before, lags slightly behind, and [N/O] increases; the ISM therefore moves up and to the left in the [N/O]–[O/H] plane. The result is an anticlockwise loop, which we illustrate for the solar circle with a black dashed line in the left-hand panel of Fig. 10. The effect is generally larger in [O/H] than in [N/O] (∼0.1 dex versus ∼0.05 dex in this example) because dilution affects both [O/H] and [N/H] similarly. In the model with oscillations in $\dot{\Sigma}_{\rm in}$, we find that qualitatively similar processes drive the evolution in abundances, but there are interesting differences in detail which we discuss below in the context of scatter in the observed trend.

In the middle and right-hand panels of Fig. 10, we plot the scatter in the gas-phase [N/O]–[O/H] relation inferred observationally by Schaefer et al. (2020). Using data from the MaNGA IFU survey (Bundy et al. 2015), they measure N and O abundances in 709 541 spaxels across 6507 unique galaxies spanning 10^9–10^{11} M$_\odot$ in stellar mass. Since our model is appropriate for Milky Way-mass galaxies, we focus our comparison on the $M_\star = 10^{10.5}$–10^{11} M$_\odot$ mass range (Licquia & Newman 2015), which cuts our sample sample to 197 787 individual N and O measurements from the MaNGA IFU spaxels. In narrow bins of [O/H], we then compute the 16th, 50th, and 84th percentiles of the [N/O] distribution. Placing the median [N/O] at Δ[N/O] = 0, the shaded regions above and below 0 in Fig. 10 denote the difference between 16th and 84th percentiles of the distribution in each [O/H] bin.

We compare both of our oscillatory variants to the width of the [N/O] distribution by over-plotting the difference in [N/O] at fixed [O/H] between our oscillatory models and their constant counterpart (i.e. the vertical offset between the solid and dotted lines in the left-hand panel, and the equivalent thereof for the oscillatory $\dot{\Sigma}_{\rm in}$ model). Both models produce offsets in [N/O] at fixed [O/H] which, as discussed above, arise as consequences of dilution, and the offsets are generally consistent with the width
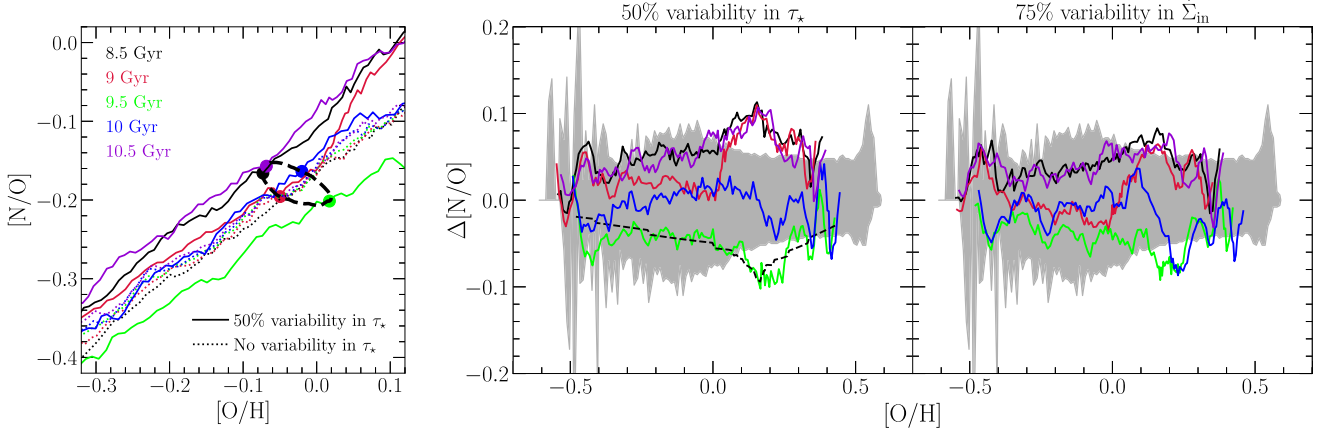
Figure 10. Left: One cycle of oscillations in the [N/O]–[O/H] relation at high [O/H] induced by sinusoidal variability in $\tau_\star$ with an amplitude of 0.5 (solid coloured lines; see equation 9). Dotted lines show the [N/O]–[O/H] relation at the same five snapshots in the fiducial model with no variability in $\tau_\star$. We use the diffusion migration prescription in both cases (see discussion in Section 3). The black dashed line shows the time evolution of the abundances at $R_{\rm gal} = 8$ kpc, the approximate Galactocentric radius of the Sun, with the times of each of the five snapshots marked by a coloured point. Middle and right: For the same five snapshots in the left-hand panel, the deviation in [N/O] at fixed [O/H] relative to the fiducial model for the case with sinusoidal variability in $\tau_\star$ at an amplitude of 0.5 (middle; see equation 10) and with sinusoidal variability in $\dot{\Sigma}_\star$ at an amplitude of 0.75 (right; see equation 10). The shaded regions in both panels quantify the width of the [N/O] distribution in $10^{10.5}$–10^{11} M$_\odot$ galaxies in MaNGA taken from Schaefer et al. (2020). In bins of [O/H], we place the median [N/O] at Δ[N/O] = 0, and the lower (upper) envelope denotes the 16th (84th) percentile of the [N/O] distribution. The black dashed line in the middle panel denotes the same quantity as the corresponding solid green line but computed from the post-processing migration prescription, which neglects the impact of stellar migration in computing enrichment rates (see discussion in Section 3).

of the relation derived observationally by Schaefer et al. (2020). This supports their argument that variations in the local SFE can drive intrinsic scatter in the [N/O]–[O/H] relation, but the effects of stellar migration are still non-negligible. We demonstrate this by comparing the green solid line in the middle panel for the $t = 9.5$ Gyr snapshot to the black dashed line denoting the same quantity with post-processing migration (see discussion in Section 3). While some of the features in Δ[N/O] as a function of [O/H] can be attributed to the difference in GCE parameters, stellar migration affects [N/O] ratios with an amplitude of ∼0.05 dex (see also Fig. 5 and discussion in Section 4.1). Although this is smaller than the impact of oscillations in either $\tau_\star$ or $\dot{\Sigma}_{\rm in}$ (∼0.1 dex), it is none the less significant compared to the width of the Schaefer et al. (2020) distributions, also at the ≲0.1 dex level; this suggests that stellar migration is a subdominant but non-negligible source of scatter.

In general, variability in $\tau_\star$ impacts abundances more strongly than variability in $\dot{\Sigma}_{\rm in}$. Fig. 10 shows similar changes in [N/O] at fixed [O/H] in both of our oscillatory variants, but it requires an amplitude of 75 per cent in accretion rates to achieve the same Δ[N/O] as an amplitude of 50 per cent in the SFE. This weaker impact arises out of an abundance response that is much more *along* the [N/O]–[O/H] relation rather than *against* it as in the oscillatory $\tau_\star$ model (see the black dashed line in the left-hand panel of Fig. 10). Both [O/H] and [N/H] vary with larger amplitudes in the variable infall model due to episodes of enhanced and suppressed accretion, but the effects of dilution on [N/H] are amplified by the combination with metallicity-dependent yields. As a result, [N/H] varies with a larger amplitude than [O/H], whereas the opposite is the case in the oscillatory $\tau_\star$ model. Consequently, [N/O] increases rather than decreases with increasing [O/H], and changes in [N/O] at fixed [O/H] are smaller. In the context of the observational results (Schaefer et al. 2020), this suggests that different [N/O] ratios at fixed [O/H] are less likely to reflect changes in the accretion rate and more likely to reflect variations in the internal properties of the

star-forming ISM, such as the thermal state or the pressure, quantities which here get folded into $\tau_\star$.

4.6 The [N/O]–[O/H] relation as an equilibrium phenomenon

As shown by Weinberg et al. (2017), under generic conditions the abundances of a one-zone GCE model with continuing gas infall evolve to an equilibrium, in which new metal production is balanced by dilution and by the loss of ISM metals to star formation and outflows. Fig. 5 shows that the [N/O] ratio at a given radius in our multizone GCE model approaches an equilibrium after $t \approx 5$ Gyr. Fig. 7 further shows that the [N/O]–[O/H] relation that emerges in our model is driven by the metallicity dependence of the N yield, with the time-delay of AGB enrichment having minimal impact. This indicates that – for the purposes of computing the equilibrium abundance of N – the AGB star DTD can be neglected, assuming instantaneous production as in Section 4.3. This allows analytical solutions to the [N/O] ratio that will arise at a given equilibrium [O/H].

For an exponential SFH, $\dot{M}_\star \propto e^{-t/\tau_{\rm SFH}}$, with instantaneous enrichment and recycling of an element X with IMF-averaged yield y_X, the equilibrium ISM mass fraction is

$$Z_{\rm eq,X} = \frac{y_X}{1 + \eta - r - \tau_\star/\tau_{\rm SFH}}, \qquad (11)$$

where (as before) $\eta = \dot{M}_{\rm out}/\dot{M}_\star$, $r \approx 0.4$ is the recycling fraction, and $\tau_\star = M_{\rm gas}/\dot{M}_\star$ is the SFE time-scale (see section 3). When an element's characteristic enrichment delay time is $\ll \tau_{\rm SFH}$, the correction to equation (11) is very small (Weinberg et al. 2017), which alongside Fig. 7 suggests that the AGB DTD of N enrichment can safely be neglected for these purposes. The [N/O] abundance ratio in equilibrium is then given by the ratio of the yields with the metallicity-dependent N yield evaluated at the equilibrium O

abundance:

$$[\mathrm{N/O}]_{\mathrm{eq}} = \log_{10}\left(\frac{Z_{\mathrm{N,eq}}/Z_{\mathrm{O,eq}}}{Z_{\mathrm{N,\odot}}/Z_{\mathrm{O,\odot}}}\right) = \log_{10}\left(\frac{y_{\mathrm{N}}(Z_{\mathrm{O,eq}})/y_{\mathrm{O}}^{\mathrm{CC}}}{Z_{\mathrm{N,\odot}}/Z_{\mathrm{O,\odot}}}\right),$$
(12)

where $y_{\mathrm{N}}(Z_{\mathrm{O}})$ denotes the *total* IMF-averaged N yield (CCSN + AGB) at a given Z_{O} as in Fig. 4. We have spot-checked this formula for each of our AGB yield models taken from the literature against the left-hand panel of Fig. 6 and found agreement to 0.02 dex or better, slightly smaller than the impact of stellar migration on gas-phase N abundances (see discussion in Sections 4.1 and 4.5).

Equation (12) can be used to predict the [N/O]–[O/H] relation for a given set of yields. Our fiducial AGB star yield (equation 3 with $\xi = 9 \times 10^{-4}$) gives an IMF-averaged yield of 9.3×10^{-4} at $Z = Z_{\odot}$ (Fig. 4; see also discussion in Section 2). Applying this value (along with $y_{\mathrm{O}}^{\mathrm{CC}} = 0.015$, $Z_{\mathrm{N,\odot}} = 6.91 \times 10^{-4}$, and $Z_{\mathrm{O,\odot}} = 5.72 \times 10^{-3}$) to equation (12) and separating the massive star contribution of $y_{\mathrm{N}}^{\mathrm{CC}} = 3.6 \times 10^{-4}$ for generality gives

$$10^{[\mathrm{N/O}]_{\mathrm{eq}}} = 10^{[\mathrm{N/O}]_{\mathrm{cc}}} + (0.513)10^{[\mathrm{O/H}]_{\mathrm{eq}}},$$
(13)

where $[\mathrm{N/O}]_{\mathrm{cc}} = -0.7$ is our empirical CCSN 'plateau' taken from Fig. 1, for which alternate values can be computed from choices regarding $y_{\mathrm{N}}^{\mathrm{CC}}$ and $y_{\mathrm{O}}^{\mathrm{CC}}$ (see discussion in Section 2.1). One can also reverse engineer equation (12) to derive the IMF-averaged N yield required to match an empirical [N/O]–[O/H] relation given a value of $y_{\mathrm{O}}^{\mathrm{CC}}$.

This analysis sharpens the conventional understanding of why [N/O] is a useful metallicity indicator in external galaxies when [O/H] cannot be measured directly. The relation between [N/O] and [O/H] is driven by stellar astrophysics (i.e., yields) in a way that is relatively insensitive to the SFH, SFE, or other galactic-scale physics. Viewing the relation from this perspective also highlights where one should be cautious about using [N/O] as a metallicity indicator. First is in environments where the stellar yields could be substantially different, perhaps because of differences in the IMF or in stellar rotation. Second is in galaxies that may be far from equilibrium, e.g., because of recent bursts of star formation or mergers diluting the ISM. The sinusoidal star formation variations considered in Section 4.5 perturb equilibrium enough to create $\sim$0.1 dex excursions in [N/O] at fixed [O/H] (Fig. 10). Third is in galaxies that are too young to have reached equilibrium. Although the [N/O]–[O/H] relation of our fiducial model is within $\sim$0.1 dex of its final value by $t = 5$ Gyr, it is lower at earlier times (Fig. 5). One-zone models with a metallicity-dependent N yield can be used to estimate whether high-redshift galaxies are likely to have reached equilibrium based on their SFRs, gas fractions, metallicities, and stellar masses. Dwarf galaxies often have low SFE and might therefore reach equilibrium more slowly. However, these galaxies are also typically in the low-metallicity regime where [N/O] is determined by the metallicity-independent primary yields anyway.

4.7 Summary

We find good agreement between GCE model predictions and the observed [N/O]–[O/H] relation if IMF-averaged N yields scale with progenitor metallicity approximately as

$$\frac{y_{\mathrm{N}}^{\mathrm{CC}}}{y_{\mathrm{O}}^{\mathrm{CC}}} = 0.024$$
(14a)

$$\frac{y_{\mathrm{N}}^{\mathrm{AGB}}}{y_{\mathrm{O}}^{\mathrm{CC}}} = 0.062\left(\frac{Z}{Z_{\odot}}\right),$$
(14b)

where the prefactor of 0.062 comes from integrating our linear model with $\xi = 9 \times 10^{-4}$ over the mass range $M_{\star} = 1$–$8\,\mathrm{M}_{\odot}$ and normalizing by $y_{\mathrm{O}}^{\mathrm{CC}} = 0.015$. The absolute scale of yields is degenerate with the strength of outflows in GCE models (see discussion in Section 4.2.1), but the ratio of $(y_{\mathrm{N}}^{\mathrm{CC}} + y_{\mathrm{N}}^{\mathrm{AGB}})/y_{\mathrm{O}}^{\mathrm{CC}}$ is well-constrained by the observed [N/O]–[O/H] trend. Motivated by the C11 + C15 AGB yields, we have assigned all of the metallicity dependence in equation (14) to the AGB component, but other $y_{\mathrm{N}}^{\mathrm{CC}} + y_{\mathrm{N}}^{\mathrm{AGB}}$ combinations with the same total metallicity dependence would predict similar trends. Reproducing one of the steeper [N/O]–[O/H] relations shown in Fig. 1 as opposed to the Dopita et al. (2016) relation would require a steeper (i.e., super-linear) metallicity dependence. However, the comparison against stellar trends in Fig. 9 instead suggests a slightly sub-linear scaling.

While a $\sim$linear metallicity dependence is all that is required to reproduce the gas-phase trends (see Fig. 7 and discussion in Section 4.3), stellar trends of [N/O] with [O/Fe] and age are sensitive to the portion of the yield attributed to AGB stars and their associated time-delay. We have success reproducing these results when the relative contribution of AGB stars follows equations (14a) and (14b) and with a characteristic time-delay of the order of $\sim$250 Myr (see Fig. 9 and discussion in Section 4.4). The C11 + C15 models imply an approximately linear mass dependence of the fractional N yield $Y_{\mathrm{N}}^{\mathrm{AGB}}(M_{\star})$. With this mass dependence and the IMF-averaged yield of equation (14b), we can write

$$\frac{Y_{\mathrm{N}}^{\mathrm{AGB}}(M_{\star}, Z_{\star})}{y_{\mathrm{O}}^{\mathrm{CC}}} = 0.06\left(\frac{M_{\star}}{M_{\odot}}\right)\left(\frac{Z_{\star}}{Z_{\odot}}\right).$$
(15)

Variations in the assumed SFH do not change the overall structure of the predicted [N/O]–[O/H] relation, instead inducing scatter about the mean trend (see Fig. 10 and discussion in Section 4.5). Our results should also not be impacted by the assumed IMF. We have examined alternate versions of Fig. 2 with different slopes of the Kroupa (2001) IMF at the high-mass end. While the normalization of $y_{\mathrm{N}}^{\mathrm{CC}}$ is impacted, the $y_{\mathrm{N}}^{\mathrm{CC}}/y_{\mathrm{O}}^{\mathrm{CC}}$ ratio is unaffected. Changes in the IMF could in principle impact the effective DTD of N production in AGB stars by adjusting the relative numbers of stars of different masses. However, gas-phase trends are insensitive to the DTD (see discussion in Section 4.3), and the stellar trends of [N/O] with [O/Fe] and age do not tightly constrain the DTD (see discussion in Section 4.4).

5 CONCLUSIONS

Building on the multizone GCE model of Johnson et al. (2021), which reproduces many observed features of the [α/Fe]–[Fe/H]-age distribution of Milky Way-disc stars, we have inferred empirical constraints on the stellar nucleosynthesis of N by comparing model predictions to observed gas-phase trends in external galaxies and stellar trends in the Milky Way disc. In our models, the gas-phase abundance at a given Galactocentric radius first evolves to higher [O/H] at roughly constant [N/O] because of primary (metallicity independent) N production, then evolves upward in [N/O] with slowly increasing [O/H] because of secondary N production that increases with metallicity (Fig. 5). The [N/O]–[O/H] relation reaches an approximate equilibrium after $t = 5$–8 Gyr, consistent with previous arguments that this relation is largely redshift independent (Vincenzo & Kobayashi 2018; Hayden-Pawson et al. 2022). This [N/O]–[O/H] relation represents a superposition of evolutionary track endpoints rather than an evolutionary track itself, similar to some explanations of the low-α disc sequence in the Milky Way (e.g. Schönrich & Binney 2009; Nidever et al. 2014; Buck 2020; Johnson et al. 2021; Sharma et al. 2021).

As our principal observational benchmark, we take Dopita et al.'s (2016) characterization of observed gas-phase abundances in external galaxies (see Fig. 1). We obtain good agreement with their [N/O]–[O/H] relation if we assume the IMF-averaged yield ratios y_N^{CC}/y_O^{CC} and y_N^{AGB}/y_O^{CC} given by equation (14). If we adopt Johnson et al.'s (2021) CCSN O yield of $y_O^{CC} = 0.015$, then the population-averaged N yields are given by $y_N^{CC} = 3.6 \times 10^{-4}$ and $y_N^{AGB} = (9.3 \times 10^{-4})(Z/Z_\odot)$. This value of y_N^{CC} is consistent with the rotating massive star models of Limongi & Chieffi (2018), and we concur with previous arguments that rotating massive stars are required to explain the [N/O] ≈ -0.7 plateau observed at low metallicities (see Fig. 1; Chiappini et al. 2003, 2005, 2006; Kobayashi et al. 2011; Prantzos et al. 2018; Grisoni et al. 2021). The AGB yield is similar in form but 3 times higher in amplitude than the models of C11 + C15.

With $y_O^{CC} = 0.015$ and $y_N^{CC} = 3.6 \times 10^{-4}$, the AGB N yields of C11+C15 and V13 must be amplified by factors of 3 and 2, respectively, to achieve agreement with the Dopita et al. (2016) [N/O]–[O/H] relation (Fig. 6). However, as predicted abundance ratios depend primarily on yield ratios, we can also obtain agreement by using the unmodified C11 + C15 or V13 yields and lowering y_O^{CC}, y_N^{CC}, and the outflow mass-loading factor by the corresponding factor. Such a change could be physically justified if black hole formation is more extensive, or the IMF steeper, than implicitly assumed by the value of $y_O^{CC} = 0.015$ (see Section 4.2.1 and Griffith et al. 2021). Other successful predictions of the Johnson et al. (2021) models, including the Galactic [O/H] gradient that is one of its basic constraints, would be largely unchanged if y_{Fe}^{CC}, y_{Fe}^{Ia}, and outflow mass loading efficiencies η were all reduced by the same factor. Alternatively, one could retain a higher y_O^{CC} and y_N^{CC} but assume that Galactic winds preferentially eject CCSN products relative to AGB products, as suggested by Vincenzo et al. (2016a). The degeneracy between the overall scaling of yields and the magnitude of outflows is one of the key sources of uncertainty in GCE models, and as a result, our investigation constrains yield ratios as opposed to absolute yields.

In contrast to C11+C15 and V13, the AGB models of K10 and KL16+K18 predict IMF-averaged yields that are decreasing or approximately flat with increasing Z (Fig. 4). In our GCE models, these yields lead to clear disagreement with the Dopita et al. (2016) trend, even when we allow reasonable variations in the metallicity dependence of y_N^{CC} (Fig. 6). There are many uncertain physical effects in AGB stellar models, so it is difficult to pinpoint a single cause for this discrepancy. In general, the most efficient N production occurs when both TDU and HBB occur simultaneously because each replenishment of C and O isotopes from the stellar core by TDU adds new seed nuclei for HBB to process in ^{14}N via the CNO cycle (Ventura et al. 2013). The distinctive metallicity dependence of the K10 and KL16 + K18 yields traces back to the simultaneous occurrence of TDU and HBB over a substantial mass range at all metallicities (Fig. 3).

All of the AGB models predict that IMF-averaged N production is dominated by stars with $M > 2\,M_\odot$ (Fig. 4). As a result, the delay-time required to produce 50 per cent of the AGB N is 250 Myr or less, shorter than the ~ 1 Gyr characteristic delay of Fe fron SN Ia. The form of the [N/O]–[O/H] relation is driven by the metallicity dependence of N yields, not by the time delay of AGB production (Fig. 7), and it can be calculated accurately from simple equilibrium arguments under most circumstances (Section 4.6, equation 12).

Vincenzo et al. (2021a) inferred the median [N/O]–[O/H] trend of Milky Way-disc stars from APOGEE abundances corrected for mixing on the red giant branch using the asteroseismic mass measurements from Miglio et al. (2021). They found good agreement with the Dopita et al. (2016) trend, our observational benchmark, so

our model is also consistent with their derived APOGEE trends. Our model also reproduces, at least approximately, two important findings of Vincenzo et al. (2021a): [N/O] exhibits little correlation with stellar age at fixed [Fe/H] for ages $\lesssim 9$ Gyr, and [N/O] declines linearly with increasing [O/Fe] at fixed [O/H] (Fig. 9). The match to these observations *does* depend on the AGB DTD, and it breaks down if we either make the AGB enrichment instantaneous or make it occur as slowly as SN Ia Fe production. This comparison also suggests that the metallicity dependence of AGB star N yields is slightly sub-linear. However, we would instead conclude that a slightly super-linear dependence is required if we had chosen a steeper [N/O]–[O/H] relation from Fig. 1.

To investigate the sources of scatter in the [N/O]–[O/H] relation, we construct variants of our fiducial model that have ~ 40 per cent sinusoidal oscillations in the SFR with a 2-Gyr period, induced by oscillations in either the SFE or the gas infall rate. The combined effects of dilution by pristine infall and metallicity-dependent N production lead to oscillations in the [N/O]–[O/H] relation comparable in magnitude to the scatter measured in MaNGA galaxies by Schaefer et al. (2020) (Fig. 10). We concur with their conclusion that variations in the SFE can plausibly explain most of the observed scatter. Johnson et al. (2021) find that stellar migration induces stochastic variations in [α/Fe] enrichment because a stellar population can migrate from its birth radius before most of its SN Ia Fe production takes place. The same effect occurs for AGB N enrichment but to a lesser extent because the shorter production time-scale (~ 250 Myr) leaves less time for migration. We find that migration leads to ~ 0.05-dex scatter in [N/O] at fixed [O/H], which is smaller than the scatter measured by Schaefer et al. (2020) but not negligible.

Our findings illustrate the value and methodology of empirically constraining stellar yields by combining general theoretical expectations with GCE modelling and observational constraints. For the case of N, we have used the expectation that massive stars and AGB stars both contribute, with the AGB contribution moderately delayed in time. The metallicity dependence of the combined population-averaged yield is tightly constrained, and it is plausibly partitioned into a massive star yield that is independent of metallicity and an AGB yield that is linear in metallicity Z and progenitor mass M. The normalization of the yield is well-constrained *relative* to the IMF-averaged O yield. The DTD predicted by our fiducial model, in concert with the Johnson et al. (2021) GCE prescriptions, leads to good agreement with the [N/O]–age and [N/O]–[O/Fe] trends for Milky Way-disc stars (Fig. 9). In future work, we plan to address similar questions regarding carbon, whose production is closely related to that of nitrogen. As this approach is extended to increasing numbers of elements, the web of yield constraints and consistency tests will become steadily more powerful, providing valuable insights on stellar astrophysics, SN physics, and the history of our Galaxy.

6 DATA AVAILABILITY

VICE is open-source software. The code which numerically integrates the Johnson et al. (2021) GCE models is also publicly available and can be found in VICE's GitHub repository. The sample of star particles from h277 is available through VICE, which will download the files automatically the first time it needs them. The rest of the data from h277 can be accessed at https://nbody.shop/data.html. Observational data taken from the literature (e.g. Dopita et al. 2016; Schaefer et al. 2020; Vincenzo et al. 2021a) will be provided upon request to the corresponding author.

REFERENCES

Adams S. M., Kochanek C. S., Gerke J. R., Stanek K. Z., Dai X., 2017, MNRAS, 468, 4968

Adelberger E. G. et al., 2011, Rev. Mod. Phys., 83, 195

Anders E., Grevesse N., 1989, Geochim. Cosmochim. Acta, 53, 197

Andrews B. H., Martini P., 2013, ApJ, 765, 140

Andrews B. H., Weinberg D. H., Schönrich R., Johnson J. A., 2017, ApJ, 835, 224

Asplund M., Grevesse N., Sauval A. J., 2005, in Barnes Thomas G. I., Bash F. N., eds, ASP Conf. Ser. Vol. 336, Cosmic Abundances as Records of Stellar Evolution and Nucleosynthesis. Astron. Soc. Pac., San Francisco, p. 25

Asplund M., Grevesse N., Sauval A. J., Scott P., 2009, ARA&A, 47, 481

Asplund M., Amarsi A. M., Grevesse N., 2021, A&A, 653, A141

Basinger C. M., Kochanek C. S., Adams S. M., Dai X., Stanek K. Z., 2021, MNRAS, 508, 1156

Belfiore F. et al., 2017, MNRAS, 469, 151

Berg D. A. et al., 2012, ApJ, 754, 98

Berg D. A., Skillman E. D., Croxall K. V., Pogge R. W., Moustakas J., Johnson-Groh M., 2015, ApJ, 806, 16

Berg D. A., Pogge R. W., Skillman E. D., Croxall K. V., Moustakas J., Rogers N. S. J., Sun J., 2020, ApJ, 893, 96

Bethe H. A., 1939a, Phys. Rev., 55, 103

Bethe H. A., 1939b, Phys. Rev., 55, 434

Bigiel F., Leroy A., Walter F., Blitz L., Brinks E., de Blok W. J. G., Madore B., 2010, AJ, 140, 1194

Bilitewski T., Schönrich R., 2012, MNRAS, 426, 2266

Bird J. C., Kazantzidis S., Weinberg D. H., 2012, MNRAS, 420, 913

Bird J. C., Loebman S. R., Weinberg D. H., Brooks A. M., Quinn T. R., Christensen C. R., 2021, MNRAS, 503, 1815

Bland-Hawthorn J., Gerhard O., 2016, ARA&A, 54, 529

Bloecker T., 1995, A&A, 297, 727

Bloecker T., Schoenberner D., 1991, A&A, 244, L43

Bovy J., Leung H. W., Hunt J. A. S., Mackereth J. T., García-Hernández D. A., Roman-Lopes A., 2019, MNRAS, 490, 4740

Brooks A. M., Zolotov A., 2014, ApJ, 786, 87

Brooks A. M., Papastergis E., Christensen C. R., Governato F., Stilp A., Quinn T. R., Wadsley J., 2017, ApJ, 850, 97

Brunetti M., Chiappini C., Pfenniger D., 2011, A&A, 534, A75

Buck T., 2020, MNRAS, 491, 5435

Bundy K. et al., 2015, ApJ, 798, 7

Chiappini C., Romano D., Matteucci F., 2003, MNRAS, 339, 63

Chiappini C., Matteucci F., Ballero S. K., 2005, A&A, 437, 429

Chiappini C., Hirschi R., Meynet G., Ekström S., Maeder A., Matteucci F., 2006, A&A, 449, L27

Chiappini C. et al., 2015, A&A, 576, L12

Chieffi A., Limongi M., 2004, ApJ, 608, 405

Chieffi A., Limongi M., 2013, ApJ, 764, 21

Chisholm J., Tremonti C., Leitherer C., 2018, MNRAS, 481, 1690

Christensen C., Quinn T., Governato F., Stilp A., Shen S., Wadsley J., 2012, MNRAS, 425, 3058

Christensen C. R., Brooks A. M., Fisher D. B., Governato F., McCleary J., Quinn T. R., Shen S., Wadsley J., 2014a, MNRAS, 440, L51

Christensen C. R., Governato F., Quinn T., Brooks A. M., Shen S., McCleary J., Fisher D. B., Wadsley J., 2014b, MNRAS, 440, 2843

Christensen C. R., Davé R., Governato F., Pontzen A., Brooks A., Munshi F., Quinn T., Wadsley J., 2016, ApJ, 824, 57

Christensen C. R., Davé R., Brooks A., Quinn T., Shen S., 2018, ApJ, 867, 142

Conroy C., 2013, ARA&A, 51, 393

Conroy C., Graves G. J., van Dokkum P. G., 2014, ApJ, 780, 33

Cristallo S. et al., 2011, ApJS, 197, 17

Cristallo S., Straniero O., Piersanti L., Gobrecht D., 2015, ApJS, 219, 40

David L. P., Forman W., Jones C., 1990, ApJ, 359, 29

de los Reyes M. A. C., Kennicutt Robert C. J., 2019, ApJ, 872, 16

Doherty C. L., Gil-Pons P., Siess L., Lattanzio J. C., 2017, Publ. Astron. Soc. Aust., 34, e056

Dopita M. A., Kewley L. J., Sutherland R. S., Nicholls D. C., 2016, Ap&SS, 361, 61

El-Badry K., Wetzel A., Geha M., Hopkins P. F., Kereš D., Chan T. K., Faucher-Giguère C.-A., 2016, ApJ, 820, 131

Ellison S. L., Lin L., Thorp M. D., Pan H.-A., Scudder J. M., Sánchez S. F., Bluck A. F. L., Maiolino R., 2021, MNRAS, 501, 4777

Ertl T., Janka H. T., Woosley S. E., Sukhbold T., Ugliano M., 2016, ApJ, 818, 124

Frankel N., Rix H.-W., Ting Y.-S., Ness M., Hogg D. W., 2018, ApJ, 865, 96

Frankel N., Sanders J., Rix H.-W., Ting Y.-S., Ness M., 2019, ApJ, 884, 99

Frischknecht U. et al., 2016, MNRAS, 456, 1803

Gallino R., Arlandini C., Busso M., Lugaro M., Travaglio C., Straniero O., Chieffi A., Limongi M., 1998, ApJ, 497, 388

Gerke J. R., Kochanek C. S., Stanek K. Z., 2015, MNRAS, 450, 3289

Gil-Pons P., Doherty C. L., Lau H., Campbell S. W., Suda T., Guilani S., Gutiérrez J., Lattanzio J. C., 2013, A&A, 557, A106

Gil-Pons P., Doherty C. L., Gutiérrez J., Campbell S. W., Siess L., Lattanzio J. C., 2021, A&A, 645, A10

Gilroy K. K., 1989, ApJ, 347, 835

Governato F. et al., 2012, MNRAS, 422, 1231

Grevesse N., Sauval A. J., 1998, Space Sci. Rev., 85, 161

Griffith E. J., Sukhbold T., Weinberg D. H., Johnson J. A., Johnson J. W., Vincenzo F., 2021, ApJ, 921, 73

Griffith E. J., Weinberg D. H., Buder S., Johnson J. A., Johnson J. W., Vincenzo F., 2022, ApJ, 931, 23

Grisoni V., Matteucci F., Romano D., 2021, MNRAS, 508, 719

Gronow S., Collins C. E., Sim S. A., Röpke F. K., 2021a, A&A, 649, A155

Gronow S., Côté B., Lach F., Seitenzahl I. R., Collins C. E., Sim S. A., Röpke F. K., 2021b, A&A, 656, A94

Hasselquist S. et al., 2021, ApJ, 923, 172

Hayden M. R. et al., 2015, ApJ, 808, 132

Hayden-Pawson C. et al., 2022, MNRAS, 512, 2867

Heger A., Woosley S. E., 2010, ApJ, 724, 341

Hekker S., Johnson J. A., 2019, MNRAS, 487, 4343

Henry R. B. C., Worthey G., 1999, PASP, 111, 919

Henry R. B. C., Edmunds M. G., Köppen J., 2000, ApJ, 541, 660

Hopkins P. F., Kereš D., Oñorbe J., Faucher-Giguère C.-A., Quataert E., Murray N., Bullock J. S., 2014, MNRAS, 445, 581

Hurley J. R., Pols O. R., Tout C. A., 2000, MNRAS, 315, 543

Iwamoto K., Brachwitz F., Nomoto K., Kishimoto N., Umeda H., Hix W. R., Thielemann F.-K., 1999, ApJS, 125, 439

Izotov Y. I., Thuan T. X., Guseva N. G., 2012, A&A, 546, A122

Izzard R. G., Preece H., Jofre P., Halabi G. M., Masseron T., Tout C. A., 2018, MNRAS, 473, 2984

James B. L., Koposov S., Stark D. P., Belokurov V., Pettini M., Olszewski E. W., 2015, MNRAS, 448, 2687

Jenkins A., 1992, MNRAS, 257, 620

Jenkins A., Binney J., 1990, MNRAS, 245, 305

Jofré P. et al., 2016, A&A, 595, A60

Johnson J. A., 2019, Science, 363, 474

Johnson J. W., Weinberg D. H., 2020, MNRAS, 498, 1364

Johnson J. W. et al., 2021, MNRAS, 508, 4484

Karakas A. I., 2010, MNRAS, 403, 1413

Karakas A. I., Lattanzio J. C., 2014, PASA, 31, e030

Karakas A. I., Lugaro M., 2016, ApJ, 825, 26

Karakas A. I., Lugaro M., Carlos M., Cseh B., Kamath D., García-Hernández D. A., 2018, MNRAS, 477, 421

Kennicutt Robert C. J., 1998, ApJ, 498, 541

Kennicutt Robert C. J., de los Reyes M. A. C., 2021, ApJ, 908, 61

Kennicutt R. C., Evans N. J., 2012, ARA&A, 50, 531

Kobayashi C., 2004, MNRAS, 347, 740

Kobayashi C., Karakas A. I., Umeda H., 2011, MNRAS, 414, 3231

Kodama T., Arimoto N., 1997, A&A, 320, 41

Korn A. J., Grundahl F., Richard O., Mashonkina L., Barklem P. S., Collet R., Gustafsson B., Piskunov N., 2007, ApJ, 671, 402

Kroupa P., 2001, MNRAS, 322, 231

Krumholz M. R., Burkhart B., Forbes J. C., Crocker R. M., 2018, MNRAS, 477, 2716

Kubryk M., Prantzos N., Athanassoula E., 2015, A&A, 580, A126

Lacey C. G., Fall S. M., 1985, ApJ, 290, 154

Lagarde N., Decressin T., Charbonnel C., Eggenberger P., Ekström S., Palacios A., 2012, A&A, 543, A108

Larson R. B., 1974, MNRAS, 166, 585

Law D. R., Majewski S. R., 2010, ApJ, 714, 229

Leroy A. K., Walter F., Brinks E., Bigiel F., de Blok W. J. G., Madore B., Thornley M. D., 2008, AJ, 136, 2782

Leroy A. K. et al., 2013, AJ, 146, 19

Licquia T. C., Newman J. A., 2015, ApJ, 806, 96

Limongi M., Chieffi A., 2018, ApJS, 237, 13

Lind K., Korn A. J., Barklem P. S., Grundahl F., 2008, A&A, 490, 777

Linsky J. L. et al., 2006, ApJ, 647, 1106

Liu L., Gao Y., Greve T. R., 2015, ApJ, 805, 31

Lodders K., 2003, ApJ, 591, 1220

LUNA Collaboration, 2006, Phys. Lett. B, 634, 483

Maeder A., Meynet G., 1989, A&A, 210, 155

Maeder A., Zahn J.-P., 1998, A&A, 334, 1000

Maeder A., Grebel E. K., Mermilliod J.-C., 1999, A&A, 346, 459

Maiolino R., Mannucci F., 2019, A&AR, 27, 3

Majewski S. R. et al., 2017, AJ, 154, 94

Maoz D., Mannucci F., 2012, Publ. Astron. Soc. Aust., 29, 447

Marigo P., 2002, A&A, 387, 507

Martig M. et al., 2015, MNRAS, 451, 2230

Martig M. et al., 2016, MNRAS, 456, 3655

Matteucci F., Francois P., 1989, MNRAS, 239, 885

Meynet G., Maeder A., 2002a, A&A, 381, L25

Meynet G., Maeder A., 2002b, A&A, 390, 561

Meynet G., Ekström S., Maeder A., 2006, A&A, 447, 623

Miglio A. et al., 2021, A&A, 645, A85

Mihalas D., Binney J., 1981, Galactic Astronomy. Structure and Kinematics. W.H. Freeman & Company, New York, NY

Minchev I., Famaey B., Combes F., Di Matteo P., Mouhcine M., Wozniak H., 2011, A&A, 527, A147

Minchev I., Chiappini C., Martig M., 2013, A&A, 558, A9

Minchev I., Chiappini C., Martig M., 2014, A&A, 572, A92

Minchev I., Steinmetz M., Chiappini C., Martig M., Anders F., Matijevic G., de Jong R. S., 2017, ApJ, 834, 27

Mollá M., Vílchez J. M., Gavilán M., Díaz A. I., 2006, MNRAS, 372, 1069

Munshi F. et al., 2013, ApJ, 766, 56

Neustadt J. M. M., Kochanek C. S., Stanek K. Z., Basinger C., Jayasinghe T., Garling C. T., Adams S. M., Gerke J., 2021, MNRAS, 508, 516

Nidever D. L. et al., 2014, ApJ, 796, 38

Nomoto K., Kobayashi C., Tominaga N., 2013, ARA&A, 51, 457

Padovani P., Matteucci F., 1993, ApJ, 416, 26

Paxton B., Bildsten L., Dotter A., Herwig F., Lesaffre P., Timmes F., 2011, ApJS, 192, 3

Paxton B. et al., 2013, ApJS, 208, 4

Paxton B. et al., 2015, ApJS, 220, 15

Paxton B. et al., 2018, ApJS, 234, 34

Pejcha O., Thompson T. A., 2015, ApJ, 801, 90

Pérez-Montero E., Contini T., 2009, MNRAS, 398, 949

Pilyugin L. S., Vílchez J. M., Thuan T. X., 2010, ApJ, 720, 1738

Pilyugin L. S., Grebel E. K., Mattsson L., 2012, MNRAS, 424, 2316

Prantzos N., Aubert O., 1995, A&A, 302, 69

Prantzos N., Abia C., Limongi M., Chieffi A., Cristallo S., 2018, MNRAS, 476, 3432

Ramírez I., Allende Prieto C., Lambert D. L., 2013, ApJ, 764, 78

Rogers N. S. J., Skillman E. D., Pogge R. W., Berg D. A., Moustakas J., Croxall K. V., Sun J., 2021, ApJ, 915, 21

Sackmann I. J., Boothroyd A. I., 1991, ApJ, 366, 529

Sánchez S. F., 2020, ARA&A, 58, 99

Scalo J. M., Despain K. H., Ulrich R. K., 1975, ApJ, 196, 805

Schaefer A. L., Tremonti C., Belfiore F., Pace Z., Bershady M. A., Andrews B. H., Drory N., 2020, ApJ, 890, L3

Schiavon R. P., 2010, Publ. Korean Astron. Soc., 25, 83

Schönrich R., Binney J., 2009, MNRAS, 396, 203

Sellwood J. A., Binney J. J., 2002, MNRAS, 336, 785

Sharma S., Hayden M. R., Bland-Hawthorn J., 2021, MNRAS, 507, 5882

Silva Aguirre V. et al., 2018, MNRAS, 475, 5487

Skillman E. D., Berg D. A., Pogge R. W., Moustakas J., Rogers N. S. J., Croxall K. V., 2020, ApJ, 894, 138

Souto D. et al., 2018, ApJ, 857, 14

Souto D. et al., 2019, ApJ, 874, 97

Spitoni E., Silva Aguirre V., Matteucci F., Calura F., Grisoni V., 2019, A&A, 623, A60

Spitoni E. et al., 2021, A&A, 647, A73

Sukhbold T., Ertl T., Woosley S. E., Brown J. M., Janka H. T., 2016, ApJ, 821, 38

Suliga A. M., Shalgar S., Fuller G. M., 2021, J. Cosmol. Astropart. Phys., 2021, 042

Tacconi L. J. et al., 2018, ApJ, 853, 179

Tinsley B. M., 1979, ApJ, 229, 1046

van Zee L., Salzer J. J., Haynes M. P., 1998, ApJ, 497, L1

Vassiliadis E., Wood P. R., 1993, ApJ, 413, 641

Ventura P., Di Criscienzo M., Carini R., D'Antona F., 2013, MNRAS, 431, 3642

Ventura P., di Criscienzo M., D'Antona F., Vesperini E., Tailo M., Dell'Agli F., D'Ercole A., 2014, MNRAS, 437, 3274

Ventura P., Karakas A. I., Dell'Agli F., García-Hernández D. A., Boyer M. L., Di Criscienzo M., 2016, MNRAS, 457, 1456

Ventura P., Karakas A., Dell'Agli F., García-Hernández D. A., Guzman-Ramirez L., 2018, MNRAS, 475, 2282

Ventura P., Dell'Agli F., Lugaro M., Romano D., Tailo M., Yagüe A., 2020, A&A, 641, A103

Vila-Costas M. B., Edmunds M. G., 1993, MNRAS, 265, 199

Vincenzo F., Kobayashi C., 2018, MNRAS, 478, 155

Vincenzo F., Kobayashi C., 2020, MNRAS, 496, 80

Vincenzo F., Belfiore F., Maiolino R., Matteucci F., Ventura P., 2016a, MNRAS, 458, 3466

Vincenzo F., Matteucci F., de Boer T. J. L., Cignoni M., Tosi M., 2016b, MNRAS, 460, 2238

Vincenzo F. et al., 2021a, preprint (arXiv:2106.03912)

Vincenzo F., Weinberg D. H., Miglio A., Lane R. R., Roman-Lopes A., 2021b, MNRAS, 508, 5903

von Wesäcker C. F., 1937, Phys. Z., 38, 176

von Weizsäcker C. F., 1938, Phys. Z., 39, 633

Wadsley J. W., Stadel J., Quinn T., 2004, New Astron., 9, 137

Warfield J. T. et al., 2021, AJ, 161, 100

Weinberg D. H., 2017, ApJ, 851, 25

Weinberg D. H., Andrews B. H., Freudenburg J., 2017, ApJ, 837, 183
Weinberg D. H. et al., 2019, ApJ, 874, 102
Weinberg D. H. et al., 2022, ApJS, 260, 32
Woosley S. E., Weaver T. A., 1995, ApJS, 101, 181
Wyse R. F. G., Silk J., 1989, ApJ, 339, 700
Yong D. et al., 2016, MNRAS, 459, 487
Zahn J. P., 1992, A&A, 265, 115
Zolotov A. et al., 2012, ApJ, 761, 71

APPENDIX A: VICE

VICE[14] is an open-source PYTHON package designed to model chemical enrichment processes in galaxies with a generic, flexible model. With this paper, we mark the release of version 1.3.0, which presents a handful of new features:

(i) Users may select a mass–lifetime relation for stars from a list of several parametrized forms taken from the literature. Previously, only a single power law was implemented, but this formulation underestimates lifetimes for stars with masses $\gtrsim 4\,M_\odot$; now, the options include the equations presented in:

(a) Vincenzo et al. (2016b)
(b) Hurley, Pols & Tout (2000)
(c) Kodama & Arimoto (1997)
(d) Padovani & Matteucci (1993)
(e) Maeder & Meynet (1989)
(f) Larson (1974) **(default).**

Generally, chemical evolution models make similar predictions with each of these different forms of the mass–lifetime relation since they are not considerably different from one another (see the section titled 'Single Stellar Populations' under VICE's science documentation for further discussion[15]). We select the Larson (1974) form as a default within VICE because it is representative of other forms and

requires the lowest amount of computational overhead (aside from the single power-law option). This model is a metallicity-independent parabola in $\log \tau$–$\log m$ space for which we take updated coefficients from Kobayashi (2004) and David et al. (1990).

(ii) We have added two additional tables of AGB star yields sampled at various progenitor masses and metallicities: the KL16 + K18 and V13 models presented in this paper are new to VICE (see discussion in Section 2.2 for details).

(iii) We have built in the SN Ia yields presented in Gronow et al. (2021a, b). These tables include yields for double detonations of sub-Chandrasekhar mass carbon–oxygen white dwarfs at various progenitor metallicities.

Although VICE includes built-in SN and AGB star yield tables, users are not required to adopt any one of them for use in their chemical evolution models. Instead, it allows arbitrary functions of metallicity for both CCSN and SN Ia yields and functions of progenitor mass and metallicity for AGB star yields. It provides similar flexibility for additional parameters typically built into GCE models. VICE's backend is implemented entirely in ANSI/ISO C, providing it with the powerful computing speeds of a compiled library while retaining such scientific flexibility within the easy-to-use framework of PYTHON.

Requiring a Unix kernel, VICE supports Mac and Linux operating systems; Windows users should install and use VICE entirely within the Windows Subsystem for Linux. It can be installed via `python -m pip install vice`, after which `python -m vice --docs` and `python -m vice --tutorial` will launch a web browser to the documentation and to a jupyter notebook intended to familiarize first time users with VICE's API.

---

[14]Install (PyPI): https://pypi.org/project/vice
Documentation: https://vice-astro.readthedocs.io
Source Code: https://github.com/giganano/VICE.git
[15]https://vice-astro.readthedocs.io/en/latest/science_documentation/

This paper has been typeset from a TEX/LATEX file prepared by the author.